To the Graduate Council:
I am submitting herewith a thesis written by Samuel Ray Pankratz entitled "Fused Filament Fabrication of Ceramic Matrix Composite Preforms Via Thermo-Oxidative Stabilization of Polyetheretherketone." I have examined the final electronic copy of this thesis for form and content and recommend that it be accepted in partial fulfillment of the requirements for the degree of Master of Science, with a major in Mechanical Engineering.

Dr. Uday Vaidya, Major Professor

We have read this thesis
and recommend its acceptance:

Dr. Uday Vaidya

Dr. Brett Compton

Dr. Dustin Gilmer

Accepted for the Council:

Dixie L. Thompson

Vice Provost and Dean of the Graduate School

(Original signatures are on file with official student records.)

Fused Filament Fabrication of Ceramic Matrix Composite Preforms Via Thermo-Oxidative Stabilization of Polyetheretherketone

A Thesis Presented for the

Master of Science

Degree

The University of Tennessee, Knoxville

Samuel Ray Pankratz

August 2024

Dedicated to my grandfathers as role models, teaching me what it means to be a Tennessee Volunteer, a professional, and a man.

Acknowledgements

I would like to thank the support of family, friends, and colleagues during this work, and especially the guidance of my advisor Dr. Uday Vaidya. I would also like to thank my committee members, Dr. Brett Compton and Dr. Dustin Gilmer, for support and input along the way. I want to thank Dr. Greg Larsen and Dr. Corson Cramer from the Oak Ridge National Laboratory Extreme Environment Materials and Processing group for assistance in conceptualization and experimentation. I want to express gratitude for the help of Dr. Amber Hubbard from ORNL for assistance with dynamic mechanical analysis and Dr. Michael Lance from ORNL for performing fourier transform infrared spectroscopy. Also, I extend thanks to undergraduate research assistants Joshua Gilder for performing microscopy and Andrew Wells for assistance in sample manufacturing. I am also thankful for the assistance of Dr. Cody Pack for performing sample pyrolysis and assisting in the design and operation of pyrolysis facilities.

Abstract

Carbon-fiber-reinforced ceramic matrix composites (CMCs) are frequently used in applications where high thermo-mechanical loads are induced along with weight limitations. The first step of producing the fibrous preform allows the near-net shape of the final part to be formed with fibers placed in the desired orientation, typically relying on traditional polymer matrix composite (PMC) manufacturing methods. Recent work has demonstrated a new method to produce discontinuous fiber preforms through various forms of additive manufacturing including fused filament fabrication (FFF). This work uses Polyetheretherketone with carbon fibers (CF PEEK) for additive manufacturing of the carbon-rich polymer precursor. Critically, thermoplastic precursor materials suffer severe instability during pyrolysis as they move from melt to degradation. This work evaluates oxidative stabilization of the additively manufactured preform to preserve form at the macrostructural and microstructural scales. It is shown that thermo-oxidative stabilization near the melt temperature is an oxygen-dependent process that forms carbonyl groups to cross-link polymer chains and that shrinkage is anisotropic, measuring 17.89% in Y, 20.10% in Z, and 1.18% along the fibers in X. It also shown that, while thermo-oxidative stabilization can produce a viable preform, increased crosslinking does reduce permeability to evolved gases, leading to foaming and failure in pyrolysis.

Table of Contents

List of Tables

List of Figures

Introduction

Orville and Wilbur Wright made aviation history when, on December 17th, 1903, they flew the first heavier-than-air, self-powered airplane. The brothers accomplished this by building off the knowledge of Samuel Langley and Otto Lilienthal, among others, plus combining elements of propulsion, aerodynamics, control, and materials. They had a focused understanding of the overall aircraft system that contributed to a successful design, including early use of aluminum in an aircraft. Aviation technology would boom as rapid advances in all critical areas brought forth new designs capable of higher speeds, greater altitudes, and longer endurance [5].

The continued co-development of aerodynamic knowledge, manufacturing techniques, and propulsion systems pushed aircraft to long ranges with high service ceilings and even speeds in excess of Mach 2 - but this would not hold. The North American X-15 would first fly in 1959 in an effort to explore higher speeds and altitudes enabled by high-temperature nickel-based alloy construction. It would go on to break many records in the 1960s and be the first manned airplane to break into the complex hypersonic regime, commonly defined as Mach 5 or better. Missile and reentry vehicles were already studying these high speeds with rockets reaching hypersonic speeds as early as 1949 [6]. The combined efforts across high-speed aerospace systems made it apparent that survivability in such a challenging flight regime is difficult because of high structural loading and temperatures.

The hypersonic flight regime is characterized by Mach numbers above 5 where the aerothermal environment around a vehicle reaches high temperatures and pressures.

The chemistry and energy of the air itself will begin to change, moving from kinetic states to thermal and molecular states [7]. Such materials must endure the potential for oxidation and experience significant thermal gradients across acreage and through-the-thickness. This requirement for favorable specific strength at high temperatures is uniquely filled by carbon/carbons (C/C) and other ceramic matrix composites (CMC)s. Metals and monolithic ceramics are inadequate for this because metals lose significant strength at high temperatures and monolithic ceramics have low toughness. A C/C or CMC material achieves the high temperature and low thermal expansion of a ceramic, normally 0.1%-1.0% at 1100°C, with the toughness of a composite by combining dissimilar ceramic or carbon fibers in a ceramic or carbon matrix [8]. Additionally, thermal conductivity is reduced by 3-4 orders of magnitude when compared to metals [8]. This means C/C or CMC solutions are desirable both for external insulative or ablative parts and internal structural applications.

C/C composite development began during the 1950s. Development accelerated through the 1970s for defense applications including rocket nozzles and re-entry components [8]. Modern C/C have reached maturity to be used in vehicles like the Space Shuttle and for commercial applications such as friction, though needs exist for improvements to manufacturing processes in shape and speed.

In application, C/C and CMC parts either serve as a non-structural thermal protection system (TPS) or for structural, load-carrying applications in the vehicle. As Glass points out in his paper "Ceramic Matrix Composite (CMC) Thermal Protection Systems (TPS) and Hot Structures for Hypersonic Vehicles", "as we move from rocket-based to air-breathing vehicles, we need to move away from the 'insulated airplane' approach ... to a wide range of TPS and hot structure approaches" [9]. This means that C/Cs and CMCs will need new manufacturing methods and improved properties for structural and non-structural applications as vehicles become more advanced, demanding increased temperatures, exposure time, and reusability. Achieving those advances will happen in part through development of new manufacturing methods and materials for such parts.

Manufacturing CMC or C/C parts typically begins with processes common to the polymer matrix composite (PMC) world by using carbon or ceramic fibers to form a green body with a specialized preceramic, thermoset polymer matrix. The matrix then undergoes a high temperature conversion process to form a ceramic or carbon matrix preform before further processing to produce the final composite. Thermoplastics, however, are less commonly used for forming these matrices but have been used in the past [10, 11, 12]. Challenges in stability through processing have discouraged the use of thermoplastics compared to thermosetting counterparts since thermoplastics can re-melt and flow, whereas thermoset resins do not re-melt. Thermoplastics do, however, offer promising char yields worth pursuing, in the range of 30%-55%, and are well-suited for additive manufacturing (AM) [13].

AM techniques for thermoplastics, including those like polyetheretherketone (PEEK) with high char yields, have been extensively studied to produce PMCs [14, 15, 16]. These methods generally melt thermoplastic materials, sometimes with fiber reinforcement, to build parts layer-by-layer based on a computer-derived geometry without the need for unique tooling. This means AM can more rapidly, and at lower cost, manufacture geometries which traditional methods do not allow for [17].

AM has already been used to produce CMCs with methods including stereolithography (SLA), direct ink write (DIW), and binder jet additive manufacturing (BJAM), but these methods have limited control on fiber orientation, fiber content, and part size [18]. More recent methods use melt deposition of high-char thermoplastics to produce CMC preforms, but still suffer the poor stability in pyrolysis that has long held thermoplastic precursors behind thermosets [13, 19].

This work focuses on harnessing the benefits of AM, specifically fused filament fabrication (FFF), and PEEK to manufacture CMC preforms by addressing poor stability with thermo-oxidative stabilization. This stabilization process uses the thermally-induced degradation and oxidative cross-linking of PEEK to reduce melt instability during pyrolysis.

Chapter 1

Literature Review

1.1 Composites

Composite materials consist of two or more distinct materials combined to achieve material properties otherwise unobtainable from either material independently. The typical composite is thought of as a fiber reinforcement combined with and suspended in a matrix material. The fibers provide strength and attenuate crack propagation while the matrix holds the system together. Many combinations and applications for composites exist, each with varying fiber type, fiber length, fiber orientation, matrix type, interfacial strength, and thermal properties, among others.

Composite materials are often employed in high-performance applications demanding one or more performance characteristics generally unavailable through alternative material options. This could mean targeted specific strength, geometric constraints, or thermal properties [20] Thermal requirements for components may include functionality at high temperatures like that of the reusable carbon/carbon (RCC) leading edge portions of the Space Shuttle. In this case, the Space Shuttle used a carbon matrix composite to shield the shuttle's exterior from extreme temperatures during reentry. These temperatures would exceed 1650°C at peak, leading to high local heating and thermal gradients on a flight sequence to be repeated up to 100

times. The Space Shuttle used these materials as insulation from the extreme re-entry environment. The thermal protection system (TPS) had to keep temperatures below 177°C at the aluminum structure [21]. CMCs and C/Cs provided the necessary toughness, specific strength, and thermal conductivity, all with manageable thermal expansion (CTE) for these structures, where other materials either would not survive the heat flux during operation or would not meet CTE and thermal conductivity requirements.

1.2 High-Temperature Composites

High-temperature uses for composites demand fiber and matrix options with suitable strength at temperatures over 1000°C. This is not a concern for traditional carbon or SiC fibers. However polymer matrices cannot sustain these temperatures, epoxies are limited to about 120°C, polyetherimidies (PEI)s to nearly 175°C, and bismaleimides (BMI)s to 315°C [22, 23].

CMC material systems have thus been developed to suit high specific strengths with respect to temperature. The cost of such materials is high due to expensive constituent materials and processing conditions, thus restricting applications and motivation for development in less cost-sensitive markets like aerospace. Typical fibers are carbon fibers, often from polyacrylonitrile or pitch precursors, SiC, or alumina. Each would be selected to balance properties, like the high strength and excellent oxidation resistance of SiC or the thermal conductivity of certain carbon fibers. Matrix materials are likewise selected based on the combination of target properties. These often consist of SiC, alumina, silicon nitride, borosilicate glass, or carbon. Fiber volume fractions are lower than the traditional 60% to 70% of PMCs, instead ranging from 35% to 50% [24, 25].

There are generally two different types of CMCs: oxides (MgO, Al_2O_3, ZrO_2) and non-oxides (Si_3N_4, SiC, TiB_2, TiC). Oxide CMCs, while oxidation-resistant, have lower temperature tolerance but are easier and less expensive to fabricate

as compared to non-oxides. CMCs are commonly fabricated via an initial liquid phase infiltration of dry fibers or a prepreg fiber layup, followed by cure. Next, the green body will undergo sintering or pyrolysis at high temperatures where volatile compounds, including carbon monoxide, carbon dioxide, water, and hydrogen, are expelled. Subsequent densification steps such as polymer infiltration and pyrolysis, chemical vapor infiltration, or ceramic slurry infiltration follow to complete fabrication [26].

C/SiC and C/C-SiC are relatively mature CMC materials used in similar applications to C/C, such as friction and spacecraft, and share manufacturing similarities. C/SiC and C/C-SiC begin with carbon fibers and a preceramic or carbonaceous precursor before undergoing pyrolysis and some sort of densification, usually by PIP or CVI. These materials are generally selected for intense oxidative environments since SiC is significantly more resistant to oxidation than carbon, which can begin to oxidize as low as 300°C, wheras SiC will not oxidize until at least 1200°C. Traditional C/C methods apply to the process, but the introduction of SiC differs. SiC can be introduced by preceramic PIP, melt infiltration, or CVI. PIP methods are common to achieve rapid densification, but lower purity reduces thermal stability, which leads CVI completing some or all of the process since it deposits high-purity, thermally stable SiC. Melt infiltration uses the existing carbon in the preform to react with melted silicon, thus forming SiC regions along with carbon and silicon-rich regions. This method is perhaps the most rapid since it is not a cyclic process, but the heterogeneity in the matrix is often undesirable, and melted silicon can react with the carbon fibers leading to unwanted conversion of reinforcement fibers [27, 28].

1.3 Carbon/Carbon Composites

C/C is a better-understood CMC with well known manufacturing processes and established industry acceptance. C/C composites consist of carbon fiber reinforcement in a carbon matrix. The fibers provide strength to the material while the matrix

holds the system together. Toughness improves from a monolithic carbon due to the intermediate interfacial strength between fiber and matrix. The fibers may be discontinuous or continuous in length scale [2]. Woven continuous fibers are most common, often in 2D geometry, though 3D C/Cs are used in applications where 2D interlaminar properties are inadequate and so-called 2.5D laminates can be created with pinning or stitching in the Z direction [29].

Manufacturing a C/C composite is generally a time and energy-intensive process since, unlike PMCs, the carbon matrix cannot be directly established and must undergo energy and time-intensive post-processing. The process can take several pathways from start to finish, but the general idea is to use an initial carbonaceous preform material, which then undergoes pyrolysis steps to slowly build up the carbon matrix to a targeted bulk density. Figure 1.1 shows the common manufacturing paths for C/Cs. All processes will require one or more furnace cycles to high-temperature and subtractive processing from near-net shape to net shape [8].

1.3.1 Preforms

The preform is the foundation of the CMC, specifically C/C, where research in preform manufacturing is extensive. All preforms have a fibrous network in the near-net shape of the final part. For a C/C, these fibers are either carbon fiber or oxidized precursor fibers which are converted to carbon fibers during processing. The preform may or may not be held together with a polymer matrix material depending on the planned path forward. If the preform does use such a precursor matrix, a high char polymer resin is used in traditional PMC processing methods before a carbonization step meant to convert the resin from organic to inorganic carbon. This preform is then carried on to subsequent postprocessing methods before the final C/C is achieved [30].

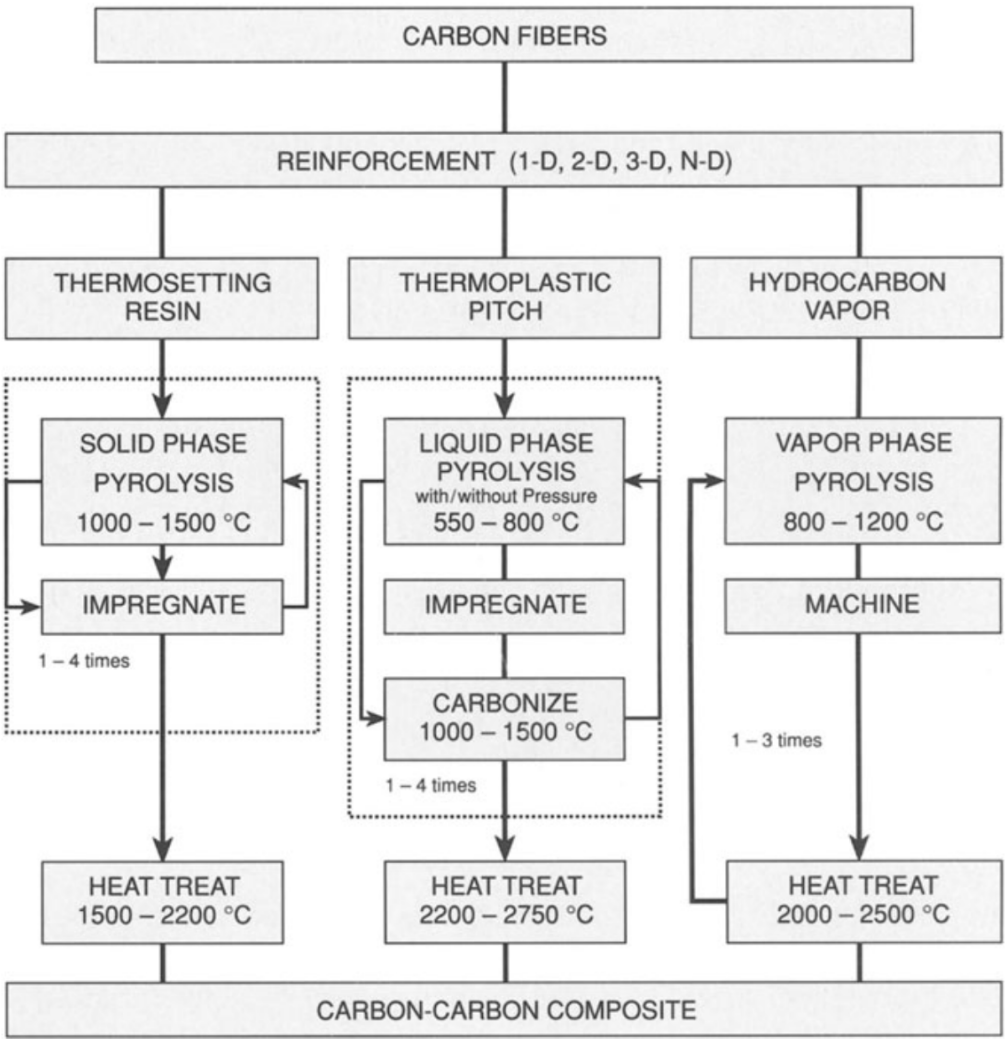

Figure 1.1: Diagram of C/C Production Methods showing the different paths from fiberous preform to final C/C through either liquid or solid phase PIP, or CVI [2].

1.3.2 Postprocessing

Postprocessing of the preform is necessary since the preform has shape but not strength due to little or no matrix material holding the system together. These densification steps aim to deposit carbon or some other ceramic material in the void space through a few modes depending on material, time, and density constraints. Subtractive machining or grinding is often carried out during these stages to bring the near net shape component to final dimensions. It is also important to note there are some precursors like pitches which form adequate density and little to no open porosity in the first pyrolysis, and as such, do not require densification steps.

Polymer Infiltration and Pyrolysis

Polymer infiltration and pyrolysis (PIP) is a common method of CMC densification, especially for forming high-density materials desired for structural applications. The polymer infiltration portion involves filling the voids of the preform with a liquid polymer resin that is subsequently cured and then pyrolyzed. Preforms for this step generally enter in the first carbonized (C0) state from an initial precursor polymer. Infiltration polymer resins like phenolic or polybenzoxazine are then similarly used because of high char yield to fill porosity after carbonization. However, the requirement for reduced viscosity to permeate small voids during the infiltration impacts the final char compared to undiluted resin. The PIP process is not restricted to only carbon precursors and can be used for formigng other matrices, such as silcon carbide, via the pyrolysis of polycarbosilane-based resins.

Mechanically, the process uses a pressure difference to force the liquid resin into the porous preform. Establishing that pressure difference generally consists of vacuum at a minimum and may be accompanied by additional pressure beyond that. The vacuum pressure draws out air from the preform's void spaces and any trapped gas in the resin. The resin is then introduced to the preform through a bagged setup akin to resin transfer molding (RTM) or in an open part. Next, pressure can be

applied to promote further infiltration. The preform is subsequently removed and passed through cure, followed by pyrolysis steps before beginning the cycle anew. This process often requires 4 to 6 cycles to reach full density.

The pyrolysis component is important to the microstructural and macrostructural properties of the composite both during and after processing. Pyrolysis, sometimes called carbonization, is a heat-treating process that runs up to 1000°C or, depending on the resin, up to 1200°C. This process is run in an inert environment, often nitrogen or argon, to avoid the oxidation and loss of material. Graphitization occurs in the 2200°C to 3000°C range, also under inert conditions. Graphitization can help open cracks during cycles and also works to increase the graphitic structure of carbon groups in the matrix. The transition from amorphous to aligned graphitic structure increases the modulus and thermal conductivity of the carbon matrix. Not all precursors provide graphitizable carbon. Carbonization and graphitization can occur under high pressures on the order of 100MPa to increase carbon yield [30, 31, 32].

Chemical Vapor Deposition

Chemical vapor deposition (CVD) or chemical vapor infiltration (CVI) is an alternative method of depositing carbon in a preform where a careful temperature and pressure gradient are combined with flowing carbonaceous gas such as methane. This process requires maintaining control of these variables inside a furnace for extended periods of time. This process might be prohibitively slow for parts of significant size since there is a risk of closing off internal voids, leading to large amounts of closed porosity and poor strength. CVD is generally applied to volume production for parts like brake rotors and is not known to produce parts of high density, meaning the 1.8g/cc to 2.0g/cc range, often associated with leading-edge components. CVD may also require the removal of a built-up scale on the part's exterior at one or more intervals [2, 8, 20].

Other Methods

Other methods of densification exist for these C/C and CMC parts. Melt infiltration is a common method used to produce C/SiC and C/C-SiC, where a carbonaceous preform is packed with silicon that is then melted to infiltrate the preform. The most common form of melt infiltration is with silicon, where the silicon reacts with carbon to produce silicon carbide in the matrix. Other methods of molten metal infiltration that can be used as well [19, 33, 34].

1.4 Carbon Precursor Matrices

Both thermoset and thermoplastic carbonaceous precursor polymers can be used to form the carbon matrix portion of the C/C CMC. Each has varying advantages, for example a thermoplastic can be remelted since no chemical bonds are formed during solidification. Both types are used as precursor resins, with some differences in behavior and acceptance.

1.4.1 Thermosets

Thermoset polymer resins are the most common precursor resins for C/Cs since high char yield is accessible and structure is well maintained through degradation. In the preform state, structural reliability is helpful to macrostructural stability. Subsequent densification steps benefit from the wide available viscosity range of resins to access small cracks and voids.

Typical resins for carbon preforms are phenolics, benzoxazines, and cyanate esters, among others. These resins are characterized by high char yields and irreversible crosslinking during cure. This permanent solidification is notable since the structure is more easily maintained during thermal degradation [2, 8, 20, 35].

1.4.2 Thermoplastics

Thermoplastics have also been used as carbon matrix precursors. Pitches have been used as the chief thermoplastic material in the world of C/Cs because of their high char yields and compatibility with graphitization [11, 13, 36]. However, the critical issues faced with these materials are associated with melt behavior starting around 300°C and moving to degradation above 400°C, making shape difficult to retain during the critical carbonization process which runs up to 1200°C [13, 19]. This necessitates other forms of stabilization, such as high-pressure carbonization, mechanical constraints, or some other form of stabilization. Carbon fiber production, for example, commonly uses polyacrylonitrile (PAN) or pitch materials with an intermediate oxidative stabilization step before carbonization [37].

Literature provides results for the use of a number of thermoplastics as precursor matrices for CMCs. Polyetheretherketone (PEEK) and materials from the same family as polyaryletherketone (PAEK) and polyetherketoneketone (PEKK) have been used along with polyetherimide (PEI) and polyphenylene sulphide (PPS). Even polyimides and polyamides have been used [8, 10, 11, 13, 38, 39, 40, 41, 42].

PEEK is a well-studied thermoplastic for composite and monolithic applications in aerospace, biomedical, and chemical industries due to excellent chemical resistance, high-temperature performance, low off-gassing, and biocompatibility [43, 44, 45]. This means PMC manufacturing of PEEK is well understood, and high-quality AM parts can be fabricated using CF PEEK. Yet, the bridge to CMC conversion has not been explored in such detail [15, 46, 47].

1.5 Oxidative Treatment of PEEK

The relevance of PEEK to a range of processing techniques and applications has motivated several studies on changes to the polymer during exposure to elevated temperatures in oxidative and non-oxidative environments. The key changes noted

are oxidative degradation, non-oxidative degradation, and crosslinking. Thermal degradation in PEEK has been shown to increase with temperature, the presence of oxygen, and even radiation. This complex process initiates with radical formation induced through heating and proceeds in intermolecular and intramolecular processes. The basic monomer structure of PEEK is shown in Fig. 1.2, demonstrating the ketone and two ether groups key to these mechanics [3, 4, 48, 49, 50, 51, 52].

The oxidative component initiates radical formation across different bonds of the molecular structure. At temperatures beginning even below melt, these sites tend to be at an ether bond and eventually form carbonyl structures which appear at 1730cm^{-1} in Fourier Transform Infrared Spectroscopy (FTIR), along with C-O-C crosslinking bonds showing up at 1100cm^{-1}. A diagram of this process is shown in Fig. 1.3. X-ray photoelectron spectroscopy (XPS) has been used to confirm this increase in oxygen-to-carbon ratio as samples are increasingly oxidized, making the polymer more brittle through cross-linking [3]. There is an intramolecular degradation at higher temperatures initiated by radicals at either the ketone group or ether bonds which close off the ring at either the ether-to-ketone bond or inside the ketone group. The spun-off radicals and carbonyl groups form diraticals, which begin to form aromatic rings. This, along with the original PEEK molecules beginning to condense, leads to graphitic formations, carbon monoxide loss, and ultimately char [4].

These decomposition processes occur alongside chain scission, which begins to occur at 400°C, though crosslinking remains dominant over chain scission [49]. At lower temperatures, oxidation is the dominant mechanic. Polymer chains are broken, and hydrogen is lost. At a constant temperature, this will continue, and the melting point will decrease. An inflection point will be hit where the melting point begins to increase as crosslinking occurs. This crosslinking increases with temperature until char begins, at which point the intramolecular processes overtake as the dominant process [3].

There are also optical changes in PEEK. The material will begin to darken and brown as it degrades, a clear indication of chemical changes. This gradient can be seen

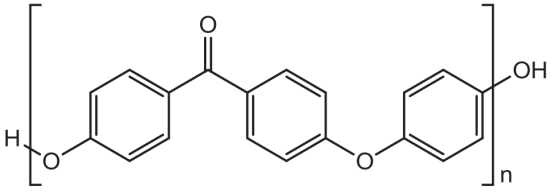

Figure 1.2: Structure of PEEK monomer showing aromatic chemical structure of two ether groups and a ketone group [3].

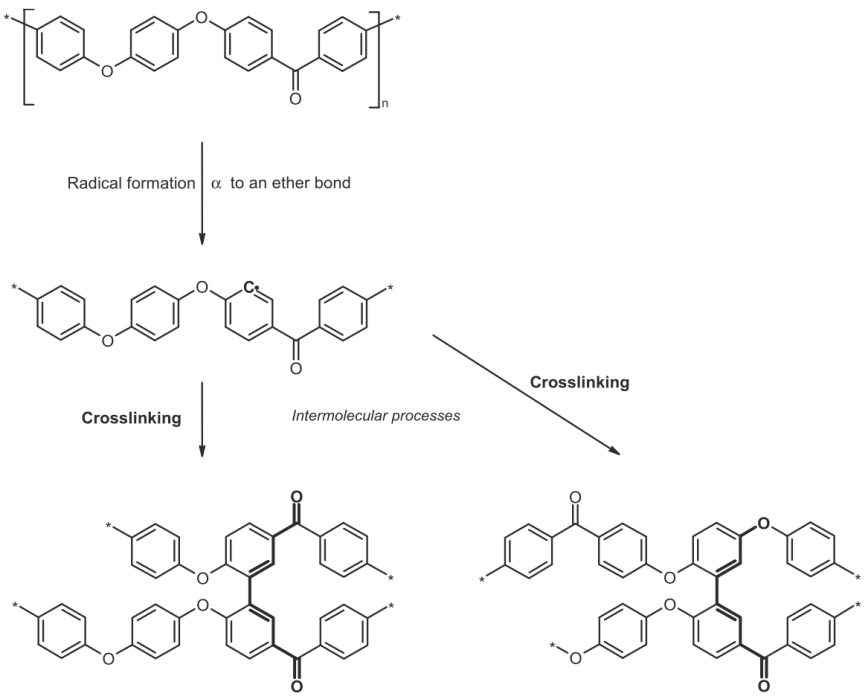

Figure 1.3: Intermolecular degradation and crosslinking in PEEK with radical formation leading to carbonyl structure formation and polymer cross-linking [4].

in cross-sections which show a clear outer skin, transition area, and bulk material. Higher temperatures create this skin faster, which leads to a smaller intermediate layer and an overall thinner oxidatively degraded zone since oxygen can no longer permeate the protective skin [3, 4].

It has been shown that the oxidative crosslinking effect in the polymer pushes the glass transition (T_g) higher. Degradation also decreases crystallinity, as shown by the minimization of melt peak area for samples at higher temperatures and durations [4]. Other studies have shown similar spectroscopic changes in PEEK aged in air and carbonyl formations at 1715cm^{-1} and 1745cm^{-1} from crosslinking via gamma radiation [3, 49].

FTIR showed peak changes at 1100cm^{-1} in the ether region, a decrease in the phenyl band around 1300cm^{-1}, and carbonyl structure formation in the 1730-1750cm^{-1} frequency range [4]. Other studies have shown similar spectroscopic changes in PEEK aged in air and carbonyl formations at 1715cm^{-1} and 1745cm^{-1} from crosslinking via gamma radiation [3, 49]. Carbonyl peaks have also been demonstrated to form under high-temperature degradation in inert environments at 1711cm^{-1} and grow with increased dwell time and temperature. In an air environment, the same peak is seen alongside a new peak developing at 1739cm^{-1}. Interestingly, the 1711cm^{-1} to 1739cm^{-1} peak ratio increases with temperature. This suggests two similar carbonyl structure formations with different activation energies and only one requiring free oxygen participation [48].

1.6 Additive Manufacturing for Ceramic Matrix Composites

AM processes have been implemented for a variety of C/C and CMC materials of different scales and geometries. AM provides the opportunity for tool-free manufacturing to drive cost and time savings. It can also allow geometries

unachievable by traditional methods, including tailored lattice structure and complex internal cavities [18, 53]. SLA, DIW, and BJAM have all been demonstrated for these materials [53, 54, 55]. These and other AM methods all vary in material, capability, and maturity [18]. Melt deposition methods have also attracted attention with several recent papers evaluating a range of thermoplastics, fibers, and print methods.

1.6.1 Common Additive Manufacturing Methods

SLA is a vat photopolymerization process which uses photo-reactive ceramic slurry to manufacture a green body by curing discrete, successive layers of resin with ultraviolet light. The part goes through a debinding and sintering process after printing. Reinforcements for these parts include fillers such as carbon nanotubes and silicon nitride fibers as well as chopped carbon fibers. Resins, however, must balance material loading since darker resins limit depth of cure. Shrinkage is also a consideration for these materials during debinding, though the introduction of reinforcement materials has shown to decrease the extent [54].

DIW is another common slurry-based AM method for CMCs. DIW extrudes a ceramic-loaded or preceramic paste through a nozzle to build the part layer-by-layer. Parts again go through a multi-step post process cycle to yield the final CMC. DIW does allow for the a wide range of reinforcements including continuous fibers. Resolution, however, is poor compared to other AM methods. The most restrictive aspect to DIW is the relationship between ink and processing since the material must be printable trough the extruder, but also stable enough to support the weight of successive layers during print [55].

BJAM uses a sprayed binder material to bind together successive layers of powder. The green body parts then go through curing, debinding, sintering, and possibly infiltration, processes. Common filler and fiberous materials are used as reinforcements, though there is an upper limit on fiber aspect ratio. Much like other

methods, feedstock restrictions exist alongside those of geometric accuracy and size [53].

1.6.2 Prior Melt Deposition Methods

Melt deposition methods have been used to manufacture composite parts across a wide range of sizes, resolutions, and materials including fillers, discontinuous, and continuous fibers. Improved control over fiber orientation and a larger build envelope make such processes attractive as a means of fabricating green bodies in terms of part size and material options. Recent literature provides an overview of current applications and limitations of such processes for ceramic matrix composite applications [13, 19, 34, 56].

Romero et al. evaluated short fiber reinforced pellet feedstocks of polyphenylene sulfide (PPS), polyetherimide (PEI), poly sulfone (PSU), polyetheretherketone (PEEK), and polyether sulfone (PES) for viability in producing C/C preforms via melt deposition AM. The authors screened candidate materials for char yield and dimensional stability, finding PEI and PEEK to each offer the highest char yields of the studied polymers at 56.9% and 50.6%, respectively. PPS, however, presented the greatest dimensional stability. Greater fiber loading improved stability in pyrolysis and slower heating rates were shown to improve both char and stability. The conclusion was that CF-PPS could be used to produce viable C/C parts with AM [13].

Cramer et al. used an AM-like automated fiber placement (AFP) system with continuous carbon fiber and PEEK to manufacture a preform before subsequent pyrolysis and melt infiltration to produce a C/C-SiC composite. A Desktop Metal machine was used with 3% porosity feedstock at 60% volume fraction before pyrolysis at up to 850°C for 30 minutes at 2°C/min in nitrogen. Samples demonstrated toughness with a characteristic strength of 234.91 MPa, but the study did note porosity and delamination issues in the composite. The authors note

that microstructural evolution through traditional CMC processes is consistent with literature and that the presence of resin-rich and void regions carries into the CMC, requiring process optimization of the PMC manufacturing process since these defects reduce mechanical strength. Improvements to the printing and pyrolysis stages are suggested to improve the strength and damage tolerance of the ultimate CMC [34].

Freudenberg et al. first demonstrated the use of FFF with discontinuous carbon fiber and PEEK to produce green bodies with a designed porosity before stabilization, pyrolysis, and melt infiltration steps. Mechanical, microstructural, and thermal properties were measured at various stages to form a full understanding of the processing stages. An 80% infill was used for samples with a filament feedstock of 20% by weight carbon fiber. The stabilization step held samples at 325°C for 48 hours in air, resulting in a strong crosslinking effect shown through differential scanning calorimetry (DSC). With some discrepancies, the general shrinkage was measured to be about 3% during oxidation and 20% during pyrolysis for directions normal to the fibers. Along the fiber direction, shrinkage of about 1% during oxidation and 5% to 10% during pyrolysis were measured [19].

Best et al. built on the work of Freudenberg et al. by focusing on optimization of specific surface area for effective oxidation and improved mechanical strength of the final C/C-SiC composite. The study found that printing in a 45° orientation with respect to the test specimen, nozzle diameter of 0.4mm, 100% infill, and 0.1mm layer height provided the greatest mechanical strength for final C/C-SiC samples. Dilatometer measurement of shrinkage in-plane measured 2.7% along the fibers and 13.7% normal to the fibers [56].

The literature suggests that the advantages of high-char yield thermoplastics and AM can be leveraged to produce low-cost CMC preforms. However, thermoplastic melting and off-gassing during the pyrolysis process leads to the part distorting unpredictably and beyond recognition. A method of controlled, predictable dimensional change is critical to the success of AM and thermoplastics for preform

manufacture. Thermo-oxidative cross-linking is suggested in this study as a viable means of achieving this stability.

1.7 Motivation

The seminal work of Freudenberg and Best first demonstrated the manufacture of non-oxide CMC preforms using CF PEEK on a desktop-scale printer [19, 56]. Others have produced related research on these materials, and all highlight the opportunity for freedom with AM, but also the varied stability challenges associated with thermoplastics [13, 57]. This means that a closer understanding of the cross-linking stabilization process and the microstructural evolution through processing are the areas most in need of evaluation to enable thermoplastic-based AM for CMCs.

Chapter 2

Objectives

The objectives of this thesis are as follows:

- Characterize thermo-oxidative stabilization of AM CF PEEK
- Produce a successful demonstration part

This work will provide insights into the oxidation procedure, pyrolysis procedure, and microstructure of preforms. The microstructure of these preforms at the bead level is significant since different C/C and CMC post-processing procedures favor different microstructural characteristics. Such work will advance the understanding and viability of using thermoplastic matrix precursors in the CMC landscape.

Chapter 3

Materials and Methods

In this work, CF PEEK was used to print test specimens before these specimens underwent oxidation at a constant tmperature and time with varied airflow rates and pyrolysis at different ramp rates. Samples were characterized at each stage to evaluate chemical and microstructural composition through the processing stages. Commercially available CF PEEK 1.75mm diameter filament feedstock (3DXTech, Grand Rapids, Michigan) made from PEEK resin (Victrex, Lancashire, United Kingdom) and 20%wt high modulus carbon fibers was used in this work [1]. Mechanical properties of CF PEEK are reported in Table 3.1. The material is designed for FFF and has shown success for this application in previous work [19].

3.1 Thermogravimetric Analysis

Thermogravimetric analysis (TGA) was performed with a TA Instruments Q50 thermogravimetric analyzer using platinum pans and samples of approximately 20-30mg. Samples cut directly from unprinted feedstock were run in nitrogen from room temperature to 800°C. Two more tests were run from room temperature to 400°C at 10°C/min then to 800°C at 5°C/min and from 400°C to 800°C at 2°C/min. These three runs capture the standard 10°C/min TGA rate along with lower pyrolysis rates

Table 3.1: Manufacturer-reported properties of CF PEEK [1].

Property	Unit	Value
Density	g/cc	1.39
Tensile Strength	MPa	126
Tensile Modulus	MPa	10100
Flexural Strength	MPa	145
Flexural Modulus	MPa	11200
Glass Transition Temperature	°C	143

to observe the relationship between pyrolysis rate and char yield. Each schedule was run three times to determine final char yield average and standard deviation.

3.2 Differential Scanning Calorimetry

Differential scanning calorimetry (DSC) was conducted with a Q2000 DSC (TA Instruments, New Castle, Delaware) from 30°C to 400°C. Samples were removed from the external surface of printed samples, weighed to approximately 5mg, and enclosed in hermetically sealed DSC pans. Samples were run through a heat-cool-heat cycle at 10°C/min, with data analysis coming from the first cool and second heating portions of each run to remove history-induced errors. Three runs each for samples as-printed and treated at 5 SCFH and 10 SCFH were evaluated to get average and standard deviation values. These data provide information on thermal properties of the polymer including melt temperature and melt energy, each of which help to explain the thermo-oxidative stabilization process.

3.3 Fused Filament Fabrication

FFF was conducted with a Funmat HT Enhanced printer (Intamsys, Shanghai, China) designed for high-temperature printing and capable of temperatures up to 90°C in the build chamber, 450°C at the print nozzle, and 160°C on the build plate. The printer has a print volume of 260mm(L) x 260mm(W) x 260mm(H). The material was printed on a custom carbon fiber bed prepared with nanopolymer adhesive (Vision Miner, Beaverton, Oregon) and a toolhead equipped with a 0.6mm hardened steel nozzle. Samples were sliced with Cura slicer (Ultimaker, Utrecth, Netherlands) and printed with a nozzle temperature of 415°C, a bed temperature of 135°C, a chamber temperature of 85°C, and 20mm/s print speed with 100% infill. Two sample geometries were used in the study. Samples for dynamic mechanical analysis (DMA) were printed at 60mm(L) x 10mm(W) x 3mm(H) and other samples were

printed in a larger body at 100mm(L) x 10mm(W) x 13mm(H) and machined down to cubes measuring 6mm on each side. This provides samples representative of uniform bulk-printed material with precise, repeatable dimensions beyond the capability of FFF printing. A diagram of these samples is shown in Fig. 3.1.

3.4 Oxidation

Oxidation was performed in a Lindburgh/Blue M STF55433 tube furnace (Thermo Fisher Scientific, Waltham, Massachusetts) using a 76.2mm alumina tube (MTI Corporation, Richmond, California). Compressed and dried shop air was regulated down to 207 kPa and run through a flow meter to regulate airflow through the system. Airflow rates were varied to samples, with various samples receiving airflow at 5 SCFH, 10 SCFH, 15 SCFH, and 25 SCFH. All samples were exposed to the same temperature cycle, heating from room temperature to 325°C at 3°C/min and held for 48h before cooling to room temperature once again. This temperature cycle selects 325°C both because this is the highest stable temperature before melt, and because previous literature has demonstrated effective stabilization based on this temperature and hold time [19].

3.5 Pyrolysis

Pyrolysis of both sample geometries A and B was conducted in a Lindburgh/Blue M STF55433 tube furnace (Thermo Fisher Scientific, Waltham, Massachusetts) using inert gas flow, nitrogen in this case, regulated to 138 kPa at a flow rate of 5 SCFH. Samples were placed in alumina crucibles during processing. Multiple pyrolysis rates were used for samples. Figure 3.3 plots the schedule followed for pyrolysis of samples, where each sustains a 4-hour hold at 120°C to remove any water content, then ramps to 500°C at 3°C/min. A 1-hour hold at 500°C stabilizes temperature before degradation. Different cycles then take the samples to 800°C at rates of

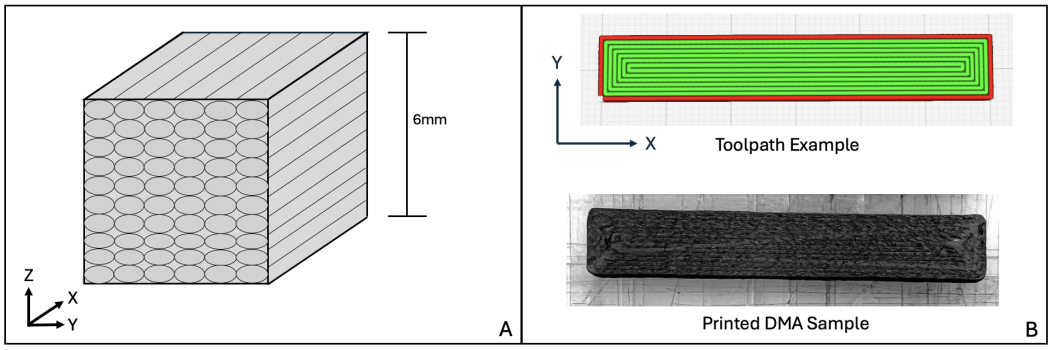

Figure 3.1: Machined down 6mm cube with print direction and fibers aligned along X-axis (A) and example toolpath along with printed DMA bar (B).

0.5°C/min, 1.0°C/min, or 3.0°C/min. Different pyrolysis rates were used to determine a relationship between pyrolysis rate and success in shape retention. Samples were also placed in different locations during processing. Figure 3.2 illustrate the locations of alumina crucibles inside the furnace where samples underwent pyrolysis in crucibles A, B, D, and E.

3.6 Optical Microscopy

Optical microscopy was performed on samples potted in Epoxicure-2 epoxy (Buhler, Lake Bluff, Illinois) and polished with a MetPrep 3 Grinder/Polisher (Allied High Tech Products, Compton, California). A VHX-5000 digital microscope (Keyence, Osaka, Japan) was used to image the samples at 200x magnification. Image analysis was conducted with ImageJ software (National Institutes for Health, New York, New York) for optical measurements.

3.7 Dynamic Mechanical Analysis

DMA was conducted with a DMA-850 (TA Instruments, New Castle, Delaware) with 35mm dual cantilever clamps and samples measuring 60mm(L) x 10mm(W) x 3mm(H) to evaluate thermo-mechanical properties of oxidized and non-oxidized samples. Three samples from each of as-manufactured, 5 SCFH, 10 SCFH, and 25 SCFH lots were tested. A temperature sweep was run from room temperature to 315°C at 10°C/min. A deflection of 10μm and frequency of 10Hz was used. Strain rates ranged from 0.0205% to 0.0228% for all samples tested. Glass transition was measured using the tangent offset intersect method which finds the intersect point from tangent lines based on linear regions before and after glass transition.

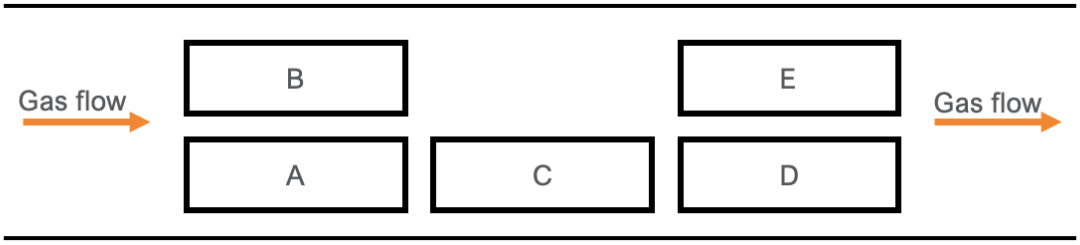

Figure 3.2: Diagram of 76.2mm diameter alumina tube furnace hot zone and alumina crucible locations A, B, C, D, and E.

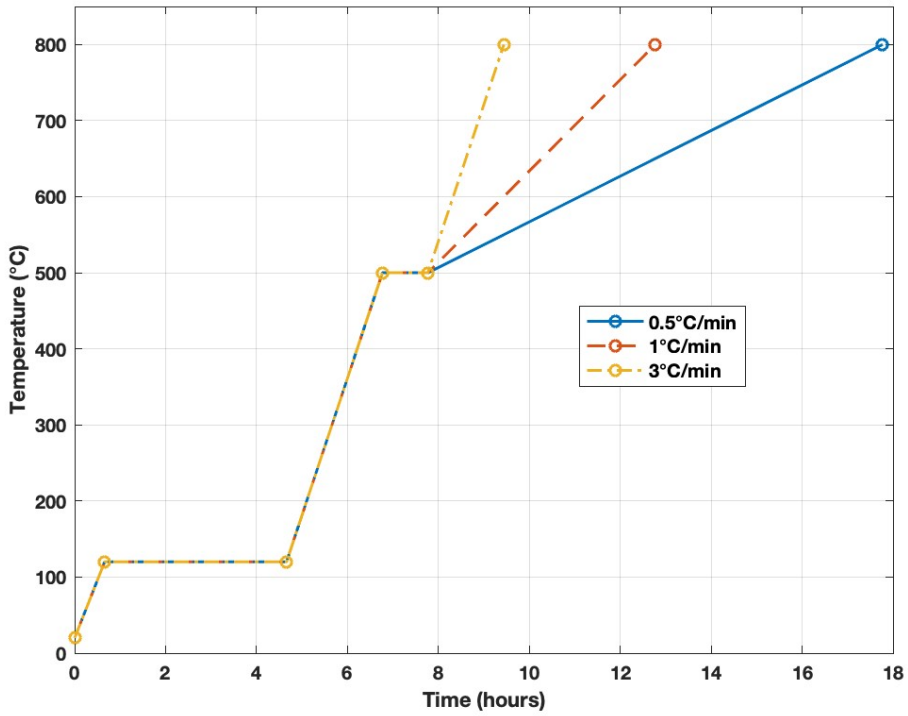

Figure 3.3: Pyrolysis schedule used for CF PEEK samples showing a 4-hour hold at 120°C, ramp to 500°C at 3°C/min, a 1-hour hold at 500°C, and ramp to 800°C at rates of 0.5°C/min, 1.0°C/min, or 3.0°C/min.

3.8 Fourier Transform Infrared Spectroscopy

FTIR was used to evaluate changes in external chemical structure of samples before and after oxidation at 5 SCFH and 10 SCFH airflow rates. FTIR spectra were acquired with a Nicolet iS50 spectrometer (Thermo Fisher Scientific, Waltham, Massachusetts) using a diamond attenuated total reflectance (ATR) stage. The diamond crystal size was 2.5 mm in diameter and the penetration depth was 0.5 to 2 µm.

3.9 Shrinkage and Density

Dimensional measurements of 6mm cube samples were taken before and after processing. A micrometer was used to measure the X, Y, and Z orientations for each of 10 total samples split between 5 SCFH and 10 SCFH oxidized samples. Mass was taken and combined with total average measurements to extract dimensional and density changes through pyrolysis. Error propagation calculations were made to determine error values for volume and density.

Chapter 4

Results and Discussion

4.1 Thermal and Chemical Characterization

Printed samples of geometries A and B were subjected to oxidative conditions at 325°C for 48h with airflow rates of 5 SCFH, 10 SCFH, and 25 SCFH and subsequently tested with DSC, DMA, and FTIR to evaluate the impact and extent of oxidation. The DMA results demonstrated an increase in storage modulus for increased oxidation across the entire temperature sweep range. Figure 4.1 shows the averaged results of 3 runs for each of the samples following these oxidation procedures. Figure 4.1 also shows the glass transition and amorphous melt regions from DMA tests in the bottom left and right, respectively. Appendix C contains the individual storage modulus versus temperature plots for each sample.

Several key differences are noted in DMA results. Oxidation did increase storage modulus from 5676 MPa to 6617 MPa, 6385 MPa, and 6344 MPa from as-printed to 5 SCFH, 10 SCFH, and 25 SCFH samples when averaged across the 50°C to 100°C range. This indicates the devlopment of cross-linked polymer at the surface of exposed portions of the samples. This does in some respect go against the hypothesis that increased airflow will increase cross-linking since the 10 SCFH and 25 SCFH samples

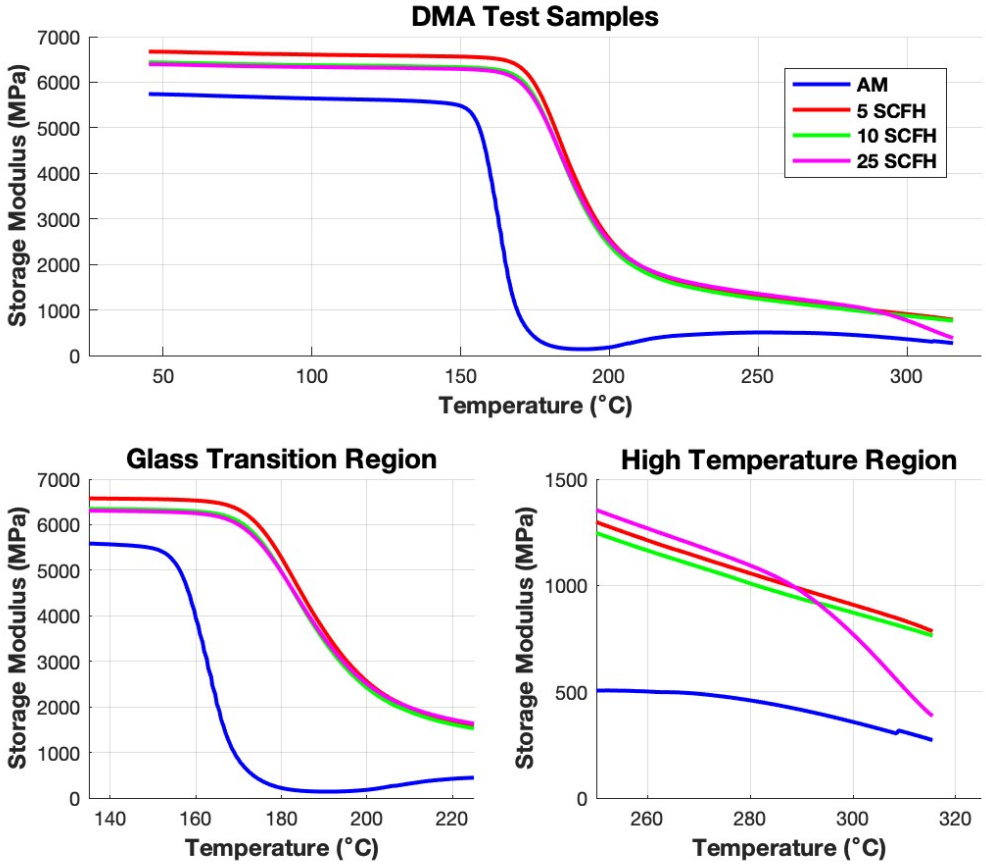

Figure 4.1: Averaged DMA results for samples as-printed and oxidized with airflow at 5, 10, and 25 SCFH.

have comparatively lower storage moduli in comparision to the 5 SCFH sample in this range below glass transition.

Figure 4.1 also provides glass transition results for the oxidized samples in the bottom left. The delayed onset of glass transition supports literature findings that glass transition will start at higher temperatures and be more gradual for increasingly crosslinked samples [4, 49]. Glass transition moved from 155.9°C to 172.2°C, 171.3°C, and 171.0°C for as-printed, 5 SCFH, 10 SCFH, and 25 SCFH oxidized samples, respectively, and became more gradual, finally linearizing closer to 225°C instead of 195°C for the as-printed samples.

Figure 4.1 shows the higher temperature region defined by amorphous melting, where a stronger linearization is shown in the oxidized samples. This suggests a resistance to melt approaching the 300°C to 315°C range. The 25 SCFH sample begins to decline more rapidly in storage modulus at 290°C. This behavior compares the the untreated sample, which clearly curves downards beginning around 250°C and never quite reaches a linear region after glass transition. The resistance to rapidly decreasing storage modulus at temperatures approaching the 325°C melt temperature echos the same trend of more cross-linked polymer on samples exposed to greater air flow as shown in DMA glass transition plots.

The sharp decline of the 25 SCFH sample at 290°C combined with a lower initial storage modulus warrants discussion since it is thought to have more cross-linking, though it does briefly hold the highest average storage modulus in the 205°C to 290°C range. These factors might indicate the oxidative cross-linking effected zone is thinner at the surface, meaning the more rapid degradation of the polymer prevented extensive activity in the bulk of the material. This would explain the lower storage modulus at lower temperatures due to less cross-linked polymer. It would also explain the sharp drop-off at 290°C, where the thinner region begins to fail and revert more closely to the bulk properties of the as-printed samples.

Characterization of the as-printed material in comparision with 5 SCFH and 10 SCFH samples was further conducted with DSC analysis. The average and standard deviation values of melt energy, melt temperature, crystallization energy, and crystallization temperature for 3 samples from each variant are shown in Fig. 4.2 and 4.1. The expected effects of oxidative degradation are again highlighed, where all values decrease as airflow, and thereby oxidative cross-linking, increase. Sample-specific plots are shown in Appendix B.

DSC was performed on small samples removed from the exterior of 6mm cube samples without any oxidation and samples oxidized with 5 and 10 SCFH. Three samples were taken from each. These data are shown in Fig. 4.2 and Table 4.1. These changes were also noted by Pascual et al. melt temperature decreased and the hot crystallization peak widened [4].

Melt temperature decreases modestly from 332.85°C to 325.21°C from as-printed to the 10 SCFH oxidized samples, and crystallization temperature from 296.79°C to 280.05°C. This melt mode makes 325°C the highest reasonable temperature for polymer stability in oxidation since the polymer will not flow and deform at such a temperature. This is why 325°C is used as the temperature for thermo-oxidative stabilization.

Melt energy falls from 10.19J/g to 5.91J/g and crystallization energy from 23.83J/g to 19.68J/g. These again highlight the impact of increasing oxidative cross-linking and the reduced participation of cross-linked regions in melt. The 5 SCFH sample falls between the average values of as-printed and 10 SCFH for all four categories.

The DSC results, though, do not describe the gradient of oxidative crosslinking through the material. This is because the samples encompass part of the gradient and do not expressly represent the external skin or internal bulk material. Precise sample dimensions vary, yet the trend of increased oxidation is still shown in these results.

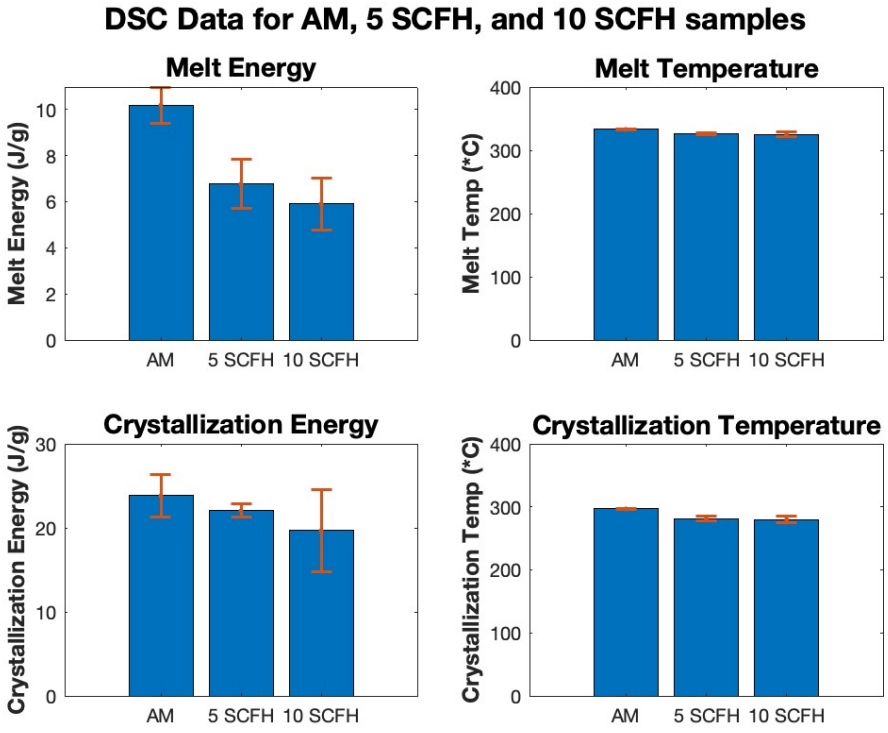

Figure 4.2: DSC results for samples as-printed and oxidized with airflow at 5 and 10 SCFH. Measured samples had a melt temperature of 332.49°C and melt energy of 12.34J/g, followed by melt temperatures of 322.10°C and 323.03°C and melt energies of 9.872J/g and 6.883J/g for 5 SCFH and 10 SCFH samples, respectively.

Table 4.1: DSC values calculated by

AM DSC				
	Melt Energy (J/g)	Melt Temp (°C)	Crystallization Energy (J/g)	Crystallization Temp (°C)
Run 1	10.12	333.05	26.65	297.06
Run 2	11.00	332.12	23.2	296.55
Run 3	9.445	333.37	21.64	296.77
Avg	**10.19**	**332.85**	**23.83**	**296.79**
StDev	**0.78**	**0.65**	**2.56**	**0.26**
5 SCFH DSC				
	Melt Energy (J/g)	Melt Temp (°C)	Crystallization Energy (J/g)	Crystallization Temp (°C)
Run 1	5.819	324.11	22.32	277.81
Run 2	7.909	327.75	21.14	284.53
Run 3	6.574	326.75	22.7	281.92
Avg	**6.77**	**326.20**	**22.05**	**281.42**
StDev	**1.06**	**1.88**	**0.81**	**3.39**
10 SCFH DSC				
	Melt Energy (J/g)	Melt Temp (°C)	Crystallization Energy (J/g)	Crystallization Temp (°C)
Run 1	4.807	325.18	14.92	279.4
Run 2	5.858	321.54	19.5	275.77
Run 3	7.073	328.91	24.61	284.99
Avg	**5.91**	**325.21**	**19.68**	**280.05**
StDev	**1.13**	**3.69**	**4.85**	**4.64**

The FTIR results from samples at 5 SCFH, 10 SCFH, and as-printed show characteristic increases with increased airflow in absorption at 1100cm^{-1}, indicating strong C-O interaction, in this case most likely oxidative crosslinking since scission of such bonds would instead decrease the peak [4]. Decreases to the phenyl band at 1300cm^{-1} and the formation of new peaks associated with oxidative degradation by the generation of carbonyl structures in the 1730-1750cm^{-1} frequency range are also shown. Specifically, the nominally flat region of the untreated sample in this frequency range shows slight increases in the 1739cm^{-1} and 1745cm^{-1} regions associated with oxidative crosslinking. The 1711cm^{-1} peak, which develops carbonyl crosslinking features without the need for free oxygen, does not appear. This matches with the literature, which describes a higher activation energy requirement for this mode of crosslinking [48]. This suggests the thermal treatment demonstrated in this process is strongly oxygen-driven crosslinking, often requiring oxygen participation, and all with limited scission. The general absorption also increases in intensity with an increase in oxidative airflow as predicted. These correlate to similar FTIR results of PEEK degraded in air demonstrated in [3, 4, 49].

These DMA, DSC, and FTIR data collectively demonstrate that increased airflow from 5 SCFH to 10 SCFH all the way up to 25 SCFH tend to increase the extent of oxidative cross-linking in samples when compared to as-printed polymer since cross-linking will increase storage modulus and cross-linked polymer chains have reduced participation in melt [4]. These data also emphasize that the process is heavily oxygen-dependent, making the atmosphere in which samples are treated important. This is all significant to reducing melt flow of the thermoplastic during degradation in pyrolysis to preserve geometry and produce a preform with predicatble shape [4].

Other forms of thermoplastic stabilization are also in the early stages of understanding for such an application. In this area, gamma radiation can cross-link PEEK [3]. Other options include mechanically constraining the preform or even an entire lack of stabilization, relying only on the inherent degradation mechanics of particular polymers and procedures [13].

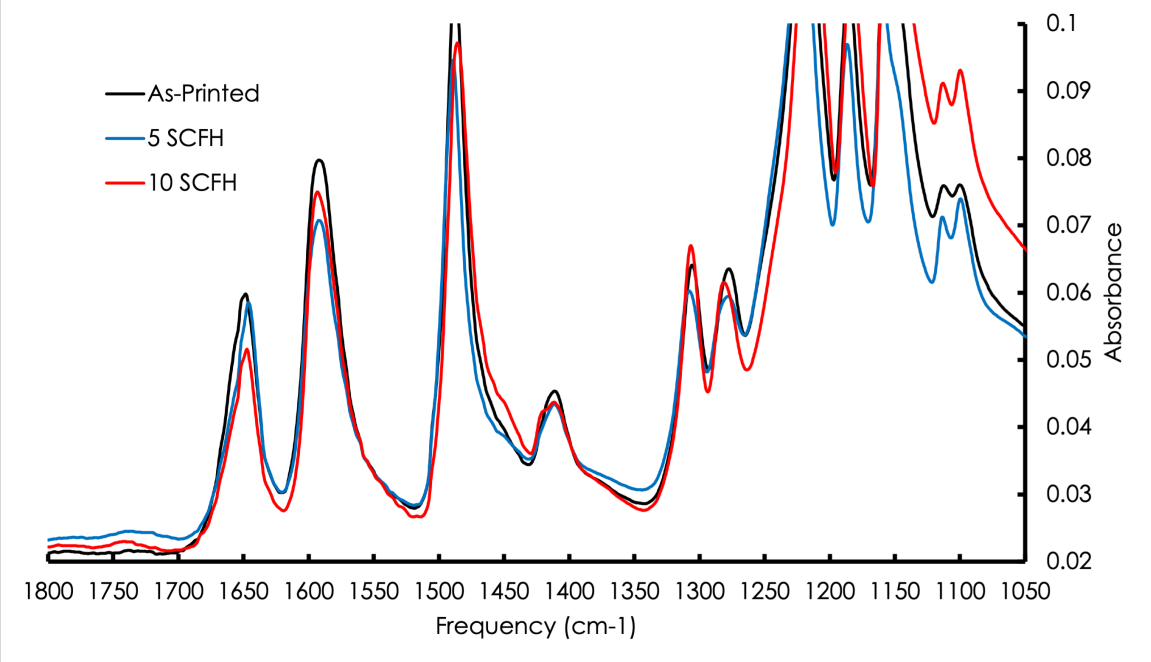

Figure 4.3: FTIR spectra for sample as-printed and oxidized with 5 SCFH and 10 SCFH flow showing decreases to the phenyl band at 1300cm^{-1} and the formation of peaks associated with the generation of carbonyl structures in the 1730-1750cm^{-1} frequency range.

4.2 Pyrolysis

TGA of CF PEEK was conducted at varied pyrolysis rates. Three runs for each schedule were taken and averaged to measure final char. The TGA plots are shown in 4.4 and represent one run for each rate. Complete TGA results are available in Appendix A. All samples started and completed the temperature ramp at similar conditions, with the final char of the 10°C/min, 5°C/min, and 2°C/min samples measuring in at averages of 59.75%, 61.85%, and 62.18%, with standard deviations of 2.39%, 0.57%, and 0.76%, respectively. These values reflect slight improvements in char for the more gradual pyrolysis rates. The onset of pyrolysis, however, did vary across samples. The 2°C/min sample began degradation around 480°C, whereas the 5°C/min and 10°C/min samples began degradation around 20°C and 30°C higher.

The standard failure mode for thermoplastics during pyrolysis is foaming as described by Romero et al., where the matrix begins to expand during degradation, causing the preform to lose shape [13]. Figure 4.5 shows this foaming failure as compared to successful pyrolysis where the green body shrinks and maintains shape. Parts may also fail partially leaving some regions foamed and others stable. These partially failed parts indicate there are FFF process-related local defects that lead to the foaming failure in pyrolysis, whereas inadequate oxidative cross-linking would be a global issue leading to global failure.

Part of this study was to evaluate the success of pyrolysis for samples of different oxidative treatments with different pyrolysis rates, where unsuccessful pyrolysis leads to foaming and expansion of the preform with large internal voids and successful pyrolysis leads to shrinkage and preservation of the printed geometry. Figure 4.6 shows the results of these trials where complete failure, partial failure, and success are denoted by red, yellow, and green. As demonstrated in the figure, greater failure was associated with samples oxidized at higher airflow rates. The samples oxidized for 48h at 325°C with 25 SCFH flow failed at a 100% rate no matter the pyrolysis schedule. Rate, however, seemed to have less of an impact on success since, for the 10 SCFH

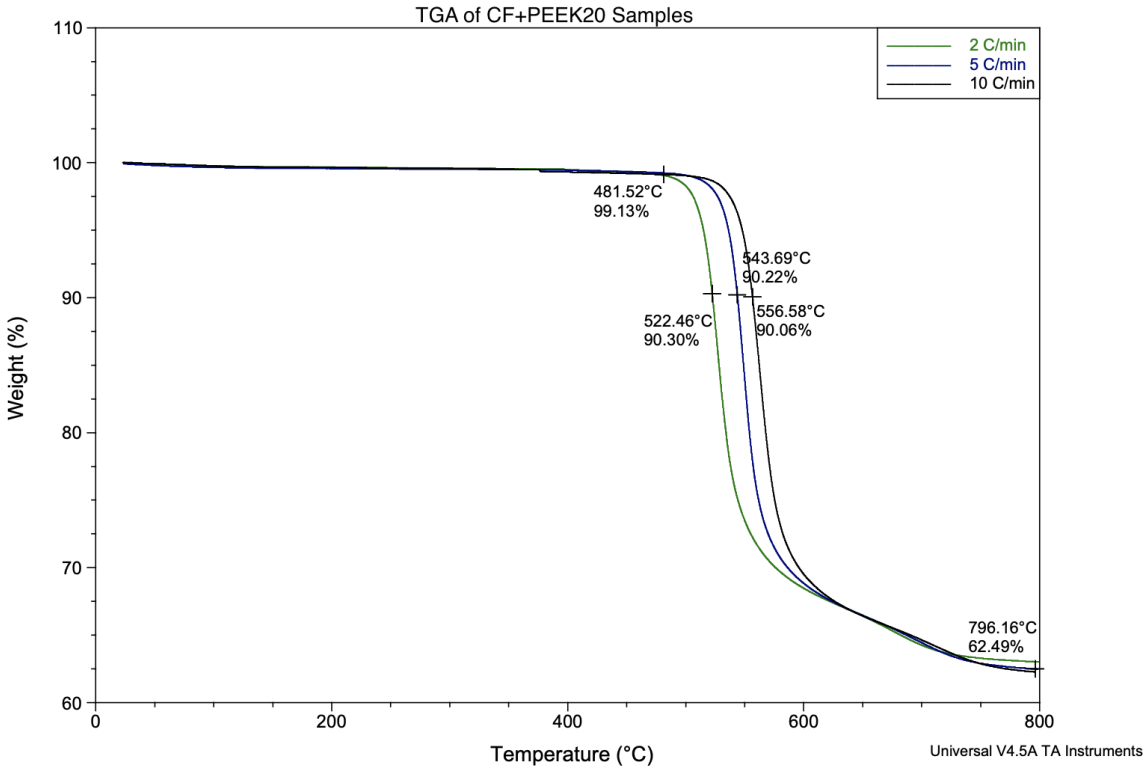

Figure 4.4: TGA plots of CF PEEK samples at 10°C/min, 5°C/min, and 2°C/min showing increased degradation onset for slower pyrolysis rates and improved final char yield of the 10°C/min, 5°C/min, and 2°C/min samples measuring in at 62.28%, 62.49%, and 63.01%, respectively.

Figure 4.5: Pyrolyzed samples (top) with polymer samples (bottom) of failed sample (left), partially failed sample (center) and successful sample (right).

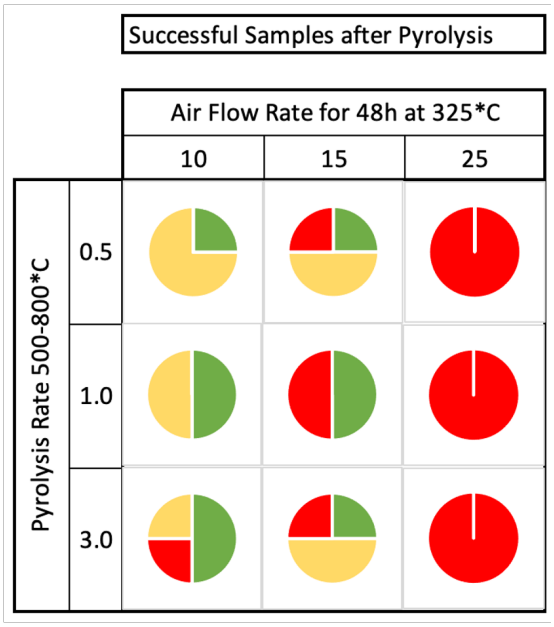

Figure 4.6: Pie charts of success (green), partial failure (yellow), and failure (red) for samples at 10, 15, and 25 SCFH and pyrolyzed at 0.5, 1.0, and 3.0°C/min. Pie charts show samples oxidized for 48h at 325°C with 25 SCFH flow failed at a 100% rate no matter the pyrolysis schedule. For the 10 SCFH and 15 SCFH samples, 25% of samples failed at both 1.0°C/min and 3.0°C/min, with slight improvement to 12.5% at 0.5°C/min. Partial failure increased for these samples from 1.0°C/min to 0.5°C/min, rising from 25% to 62.5%.

and 15 SCFH samples, 25% of samples failed at both 1.0°C/min and 3.0°C/min, with slight improvement to 12.5% at 0.5°C/min. Partial failure in fact increased for these samples from 1.0°C/min to 0.5°C/min, rising from 25% to 62.5%. It is thought that the 25 SCFH samples have a greater extent of oxidation, as supported by DMA, DSC, and FTIR, making the exterior less permeable, which prevented the escape of evolved gases and induced failure. Also of note is that location did not appear to have any effect at all, where samples in crucibles A and D did not appaer different from those in B and E. This is likely because of minimal differences in the added convective heating for samples more exposed to inert purge gases flowing through the furnace.

Dimensional change is a known and documented component of preform manufacturing [13, 18]. Measurements of the machined unidirectional 6mm cubes were taken before and after pyrolysis to measure shrinkage in the X, Y, and Z directions. Samples were oxidized with the standard cycle and either 5 SCFH or 10 SCFH of airflow. These values are presented in Table 4.2 with measurements taken per the coordinate system defined in 3.1.

Dimensional change in X, Y, and Z compare to literature, where Y and Z are normal to fiber orientation and expected to be near 20%, while X is closer to 1% [19, 56]. Measured values for 5 SCFH and 10 SCFH samples resulted in 1.18% and 1.08% shrinkage, respectively, followed by 17.89% and 18.80% for Y, then 20.10% and 20.46% for Z. Each value falls in similar domain to the alternative oxidation method counterpart, suggesting that the extent of oxidation does not have a strong impact on shrinkage during pyrolysis. Further, the mass loss of 35.80% and 35.66% for each compares with the expected mass loss of 36.99% based on TGA data, a difference of less than 2% that is attributed to a higher degradation rate, 2°C/min for TGA and 1°C/min for sample pyrolysis, and the additional impact of crosslinking on the former samples. Density changes for each have less than a 1% difference, indicating the matrix shrinks in direct proportion to mass lost.

Table 4.2: Values for dimension, mass, and density of 5 SCFH and 10 SCFH samples before and after pyrolysis. Measured values for samples resulted in 1.18% and 1.08% shrinkage, respectively, followed by 17.89% and 18.80% for Y, then 20.10% and 20.46% for Z. The mass loss was 35.80% and 35.66% and density changes for each have less than a 1% difference before and after pyrolysis.

Before Pyrolysis					
Value	5 SCFH	10 SCFH	Value	5 SCFH	10 SCFH
Avg X (mm)	6.233	6.192	StDev X (mm)	0.028	0.005
Avg Y (mm)	6.109	6.143	StDev Y (mm)	0.022	0.059
Avg Z (mm)	5.931	5.911	StDev Z (mm)	0.045	0.021
Avg Mass (g)	0.183	0.181	StDev Mass (g)	0.004	0.004
Avg Vol (cm^3)	0.226	0.225	Vol Error (cm^3)	0.002	0.002
Avg Dens (g/cc)	0.808	0.803	Dens Error (g/cc)	0.019	0.020
After Pyrolysis					
Avg X (mm)	6.159	6.125	StDev X (mm)	0.037	0.009
Avg Y (mm)	5.017	4.988	StDev Y (mm)	0.126	0.104
Avg Z (mm)	4.739	4.702	StDev Z (mm)	0.086	0.081
Avg Delta X	-1.18%	-1.08%	Delta X Error	0.73%	0.16%
Avg Delta Y	-17.89%	-18.80%	Delta Y Error	2.08%	1.86%
Avg Delta Z	-20.10%	-20.46%	Delta Z Error	1.57%	1.40%
Avg Mass (g)	0.141	0.139	StDev Mass (g)	0.004	0.004
Avg Vol (cm^3)	0.146	0.144	Vol Error (cm^3)	0.005	0.004
Avg Dens (g/cc)	0.800	0.809	Dens Error (g/cc)	0.041	0.038

4.3 Microstructure

For CMC preforms, microstructural qualities, including the fiber location, fiber orientation, void content, and microcracking, are important. Figure 4.8 shows a comparison of samples after both oxidation and pyrolysis. Each comes from the YZ plane of DMA bar samples. The whole sample at the top of the figure in micrographs A and B shows shrinkage in the matrix through the pyrolysis process. Basic optical measurements report roughly 16% shrinkage in the Z direction and 21% in the Y direction.

Beyond the scale of the part are the discrete beads that make up the part during the FFF process. Micrographs C and D in Fig. 4.8 show individual bead cross-sections before and after pyrolysis. Notably, there are prolific closed voids present in the pyrolyzed sample which persist from the printed beads themselves. Literature suggests this is a common trait of discontinuous fiber loaded PEEK, where void content can be as high as 15.8% to 22% in discontinuous CF PEEK filament feedstocks [58]. Figure 4.7 shows a micrograph of the feedstock with many small, spherical, closed voids on the order of 50μm in diameter. This is the origin of such intrabead voids in printed parts.

The matrix shrinks during pyrolysis, but the fibers do not as they are already carbonized. This shrinkage trend aligns with density meaurements which change less than 1% through pyrolysis. The pore shape and distribution from the PMC state to the CMC state is instead preserved. This lack of microstructural change is an important finding, indicating the strong connection between printed and preform microstructure.

The YZ plane does not fully represent the preform. Figure 4.9 shows a micrograph of the XZ plane along the print direction. Fiber alignment clearly follows the print direction. Voids, however, are less spherical as compared to the YZ plane. Microcracking in the matrix is also present in some localized regions but does not persist through all the matrix. These cracks clearly show access to some void regions

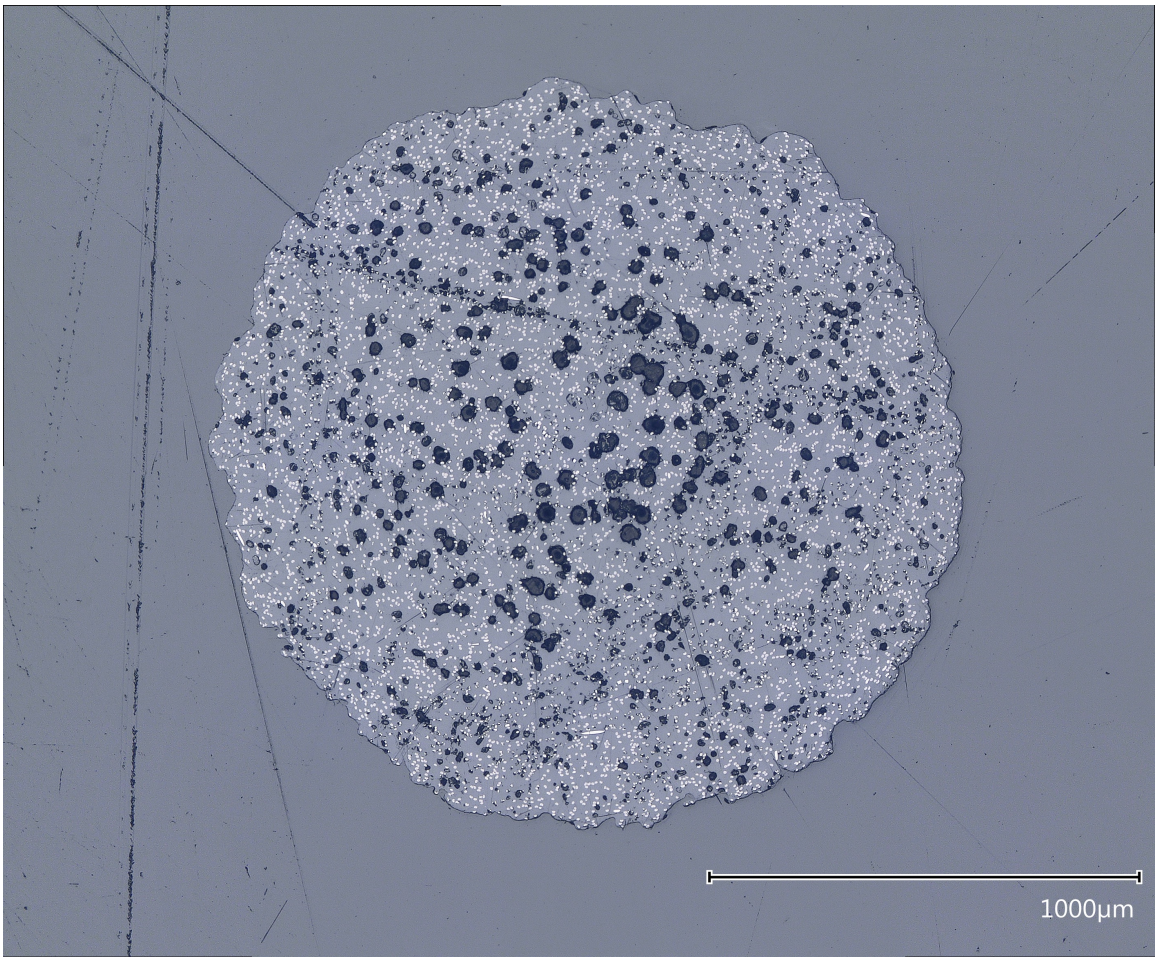

Figure 4.7: Micrograph of 1.75mm 3DXTech CF PEEK 20 feedstock showing the ditribution of fibers and voids in the matrix.

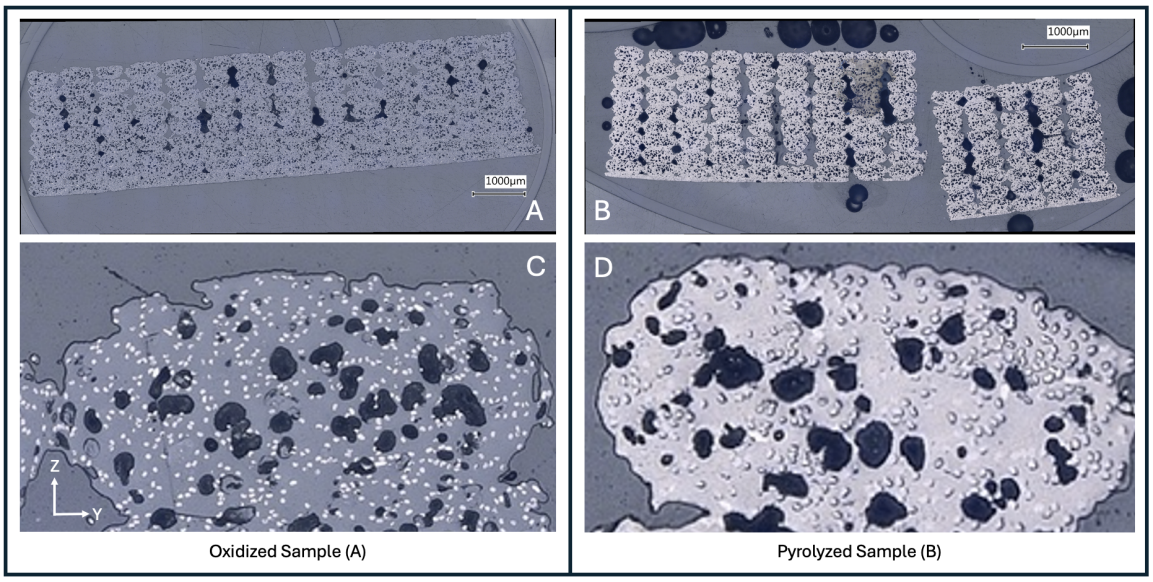

Figure 4.8: Micrograph comparison in YZ plane of oxidized sample (A) and pyrolyzed samples (B) with oxidized bead (C) and pyrolyzed bead (D) showing shrinkage and preservation of closed void content in beads through pyrolysis.

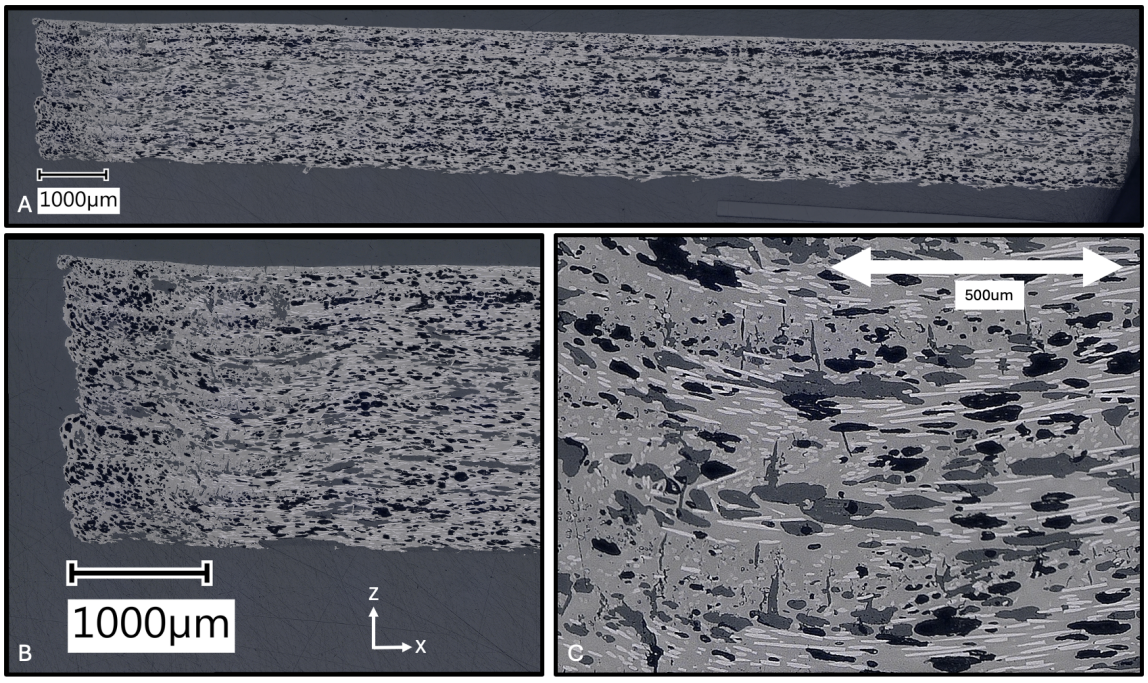

Figure 4.9: Micrographs of oxidized and pyrolyzed CF PEEK sample in XZ plane showing fiber orientation, void content, and microcracking.

in the matrix, yet still many closed voids persist. It is also important to note minimal cracking and void regions around fibers, indicating perhaps a strong fiber/matrix interface, though such a hypothesis requires mechanical failure validation to fully understand. It is thought these cracks exist normal to the fibers since fibers resist shrinkage of the matrix and force the shear-induced cracking, hence a lack of cracking parallel to any fibers [59]. There is potential to either increase or decrease the extent of such cracks based on the target process and structure of the ultimate CMC. Carbonization temperatures up to 1200°C, for instance, promote crack growth.

Not all samples pyrolyze in a stable, predictable manner. Figure 4.10 shows the YZ plane micrograph of a pyrolyzed sample, where there are clear indications of unstable pyrolysis at the lower portion of the figure. This is the bed-adjacent region during the FFF process. These closed voids form and capture volatiles generated as the polymer degrades, leading to expansion as degradation continues and gases accumulate. These first few layers in the bottom third region can be seen to have higher infill percentage denoted by fewer inter-bead voids and thereby limited exposure to oxidation. It is also known that the first few layers of a PEEK print will have increased crystallinity as compared to the bulk print [60]. It is hypothesized that either the increased infill density at this region, the increased crystallinity of the polymer, or a combination of both lead to localized instability during pyrolysis in the polymer. An increased local density would have a similar impact as increased cross-linking to reduce permeability and trap evolved gases. The imbalanced pyrolysis of this sample in the Z direction are further expressed by curling of the sample towards the top where the top region shrinks and the bottom region expands.

The large voids in the bottom third of Fig. 4.10 also points to the nature of their formation, where the voids are spherical and dark. The spherical nature implies gases from volatiles during decomposition build up to form the voids, and instead of forcing crack formation as a thermoset matrix would, casue deformation of the void space and expasion of the preform [59]. The location of the voids suggests they form from pre-existing, smaller voids given distribution similar to other closed, intra-bead

voids. The darkness of these large voids indicates they are closed since potting epoxy was unable to fill the space. The presence of these voids is problematic in two ways. The first is that expanding voids are the cause of foaming-type failure common to thermoplastic precursor matrices, indicating localized failure to maintain shape. The second is that closed voids cannot be re-infiltrated with any post-processing procedure which will impart limited strength and final density on the final CMC material [59].

These findings have a few notable impacts on the ultimate CMC. First, that the toolpath geometry will also set up the open void geometry subsequent densification steps will use to infiltrate and densify the composite. This matters because different processes like CVI and PIP are not equally effective across preforms with different permeabilities and thicknesses [2, 20]. Second, that the closed intra-bead voids persist from PMC to CMC, where it will be critical to minimize these voids since they are inaccessible and will lead to weakening of the composite [8]. Improvement to the feedstock, processing methods, or even hot isostatic pressing (HIP) after printing could be implemented to reduce such high void content and alleviate such issues in the CMC [46, 58, 61, 62]. Finally, there are multiple length scales to design for. Traditional CMCs have little more than the overall part shape and the local fiber regions to account for, whereas printed preforms like these also have the bead scale. At the bead scale there are voids in and around a particular bead, with the inner region containing fibers and closed voids, and the outer region containing bulk, unreinforced matrix. This leads to an uneven dispersion of fibers in the CMC and negative impacts on mechanical properties that fibers are meant to improve on.

The exact impact of crystallinity was not investigated as a component of this study, but forming the full body of process-product relationships for FFF and CMC preforms motivates the need for this. Crystallinity has a number of process-related causalities during FFF and additionally has implications on the cross-linking behavior, which was shown to be oxidation-driven, which creates the requirement for oxygen permeation [46]. Optical microscopy showed a potential for failure gradient based on build plate proximity, and FTIR results in this study, along with literature, suggest certain groups

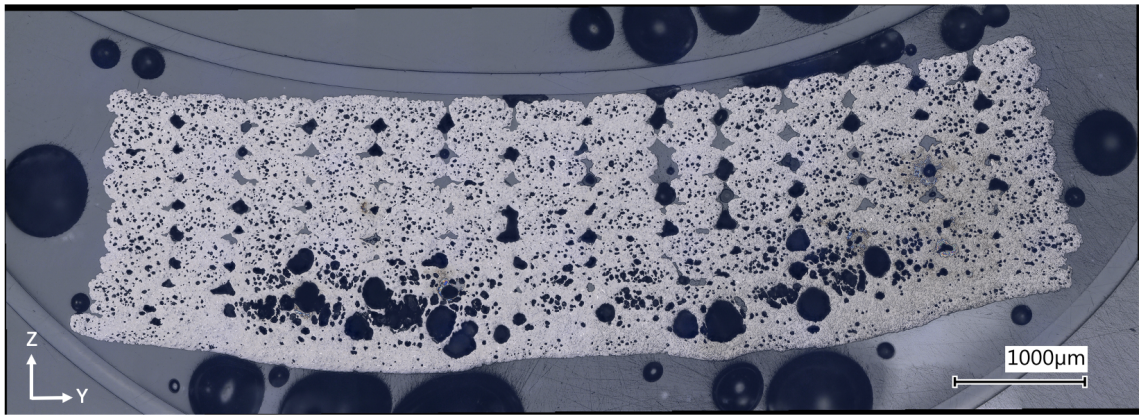

Figure 4.10: Micrograph of pyrolyzed sample showing large voids and slight foaming near build plate-adjacent area of sample.

will only form during the oxidative degradation of PEEK. Crystalline structures are known to decrease permeability through semicrystalline polymers, and thus, the impact of crystallinity on oxidative cross-linking and pyrolysis should be investigated [4].

4.4 Representative Part

A key objective of this study was to generate a representative geometry preform using the FFF process followed by oxidative stabilization and pyrolysis. A flap geometry of interest was selected by Johnson et al. as a next-generation method of producing CMC parts for spacecraft since current parts are assemblies of many CMC ribs, tubes, panels, and hardware. The implementation of AM could potentially fabricate this geometry as a single part via thermoplastic precursors and AM before conversion to a CMC, consequently saving significant time and cost. It also allows for otherwise unobtainable geometries including complex internal cavities and locally optimized densities. The concept was to print a discontinuous CF/PEEK substrate before printing continuous CF/PEEK outside of the structure and then converting the part to a C/C-SiC via pyrolysis and melt infiltration [63].

The demonstrator substrate with geometry and toolpath shown in Fig. 4.11 was first printed as shown in Fig. 4.12 before undergoing oxidation with airflow of 25 SCFH at 325°C for 48h, followed by 12h at 350°C. The overprinting process was not conducted as originally planned, allowing instead to showcase the discontinuous CF PEEK material and process for complex shapes. The part was pyrolyzed following the standard pyrolysis schedule with a 0.5°C/min rate from 500°C to 800°C.

The part shows general success potential for oxidation and pyrolysis of FFF printed discontinuous CF PEEK. The part does maintain the overall geometry of the initial green body, though matrix shrinkage as previously characterized does express through processing and was not accounted for in design. Delaminations are also visible on both faces of the part, particularly at interfaces where print orientation

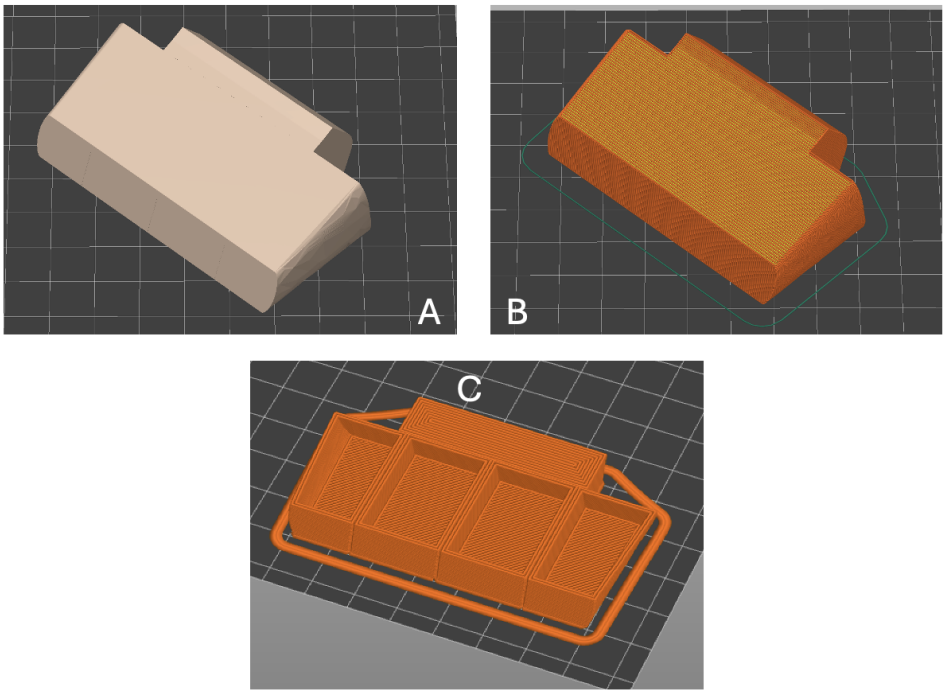

Figure 4.11: Example flap geometry model (A) with toolpath example (B) and sectioned toolpath (C) to show internal ribs and solid tab area.

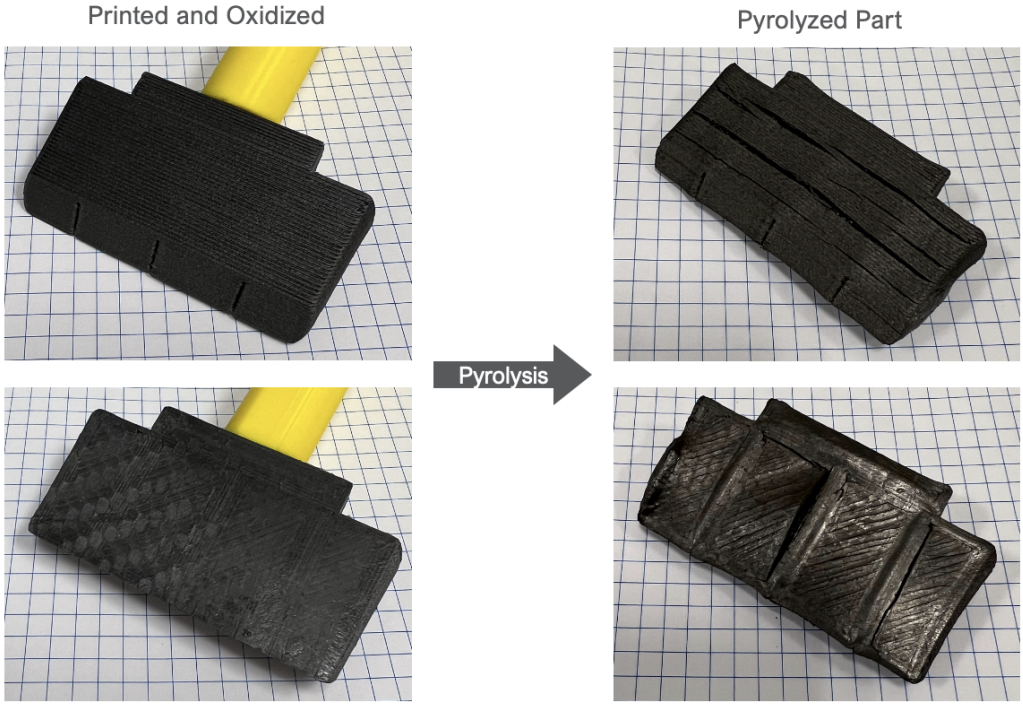

Figure 4.12: Example flap geometry before and after pyrolysis.

changes and fiber continuity is not maintained. Though toolpathing optimization and geometry could again improve on such results, this representative example stands among the best of AM thermoplastic matrix precursor-produced CMC preforms yet in literature.

Slicing parameters and toolpath optimization could be improved on the part to further improve shape retention by accounting for the anisotropic shrinkage experienced during pyrolysis. A strategy such as printing root-to-tip to maintain a more consistant transition between build plane cross-sectional areas with more symmetry would allow for advantageous use of resistance to shrink along the fibers. Additionally, AM methods like BJAM often experience similar shrinkage during debinding and sintering stages much like the changes during pyrolysis here [64]. Predictive tools could be applied to digital twin models and assist with the interlinked geometry and toolpath elements to ultimately produce samples of dimensionally-accurate post-pyrolysis parts.

Chapter 5

Conclusions and Recommendations

Critical challenges still exist for FFF as a viable process for CMCs. AM techniques, in general, have issues with defects, including porosity, poor layer bonding, and residual stresses. Fiber reinforcement also challenges the process since continuous fiber in higher volume fraction tend to produce stronger parts but also increases processing complexity.

The product of this work expands on what is known about FFF of CF PEEK for CMC preforms, being that they can be successfully formed by printing green bodies, passing parts through a thermo-oxidative stabilization step, and subsequently converting those preforms to final CMCs. The varying impact of specific oxidative stabilization steps does impact the cross-linked structure of the polymer and, critically, there likely an ideal level of cross-linking which minimizes melt and shape change during pyrolysis but does not inhibit volatiles from escaping.

Measurement of the oxidation-effected zones is a clear next step. Future work should aim to quantify the extent of cross-linking into the samples with methods like FT-IR mapping or microindentation at various points. Raman mapping was attempted in this study, but the samples were unable to return viable results due to excessive background fluorescence.

The impact of polymer crystallinity was not evaluated in this study. This is an important area to understand since there is the critical role of oxygen molecules to diffuse into the polymer at elevated temperatures to strip away an electron and open aromatic rings to cross-linking via carbonyl formation. Elevated crystallinity diminishes permeability and can reasonably be assumed to pose a factor in this process. Similarly, volatiles need to escape during pyrolysis and would again face the barrier of crystalline areas. Perhaps a comparison to an amorphous PEEK or PAEK form, or even a PEI would prove to be valuable studies.

Alternative, hybrid methods of stabilization should also be considered. Just as preforms geometry can be tailored to AM, open space and networks for a subsequent phenolic or other thermoset polymer infusion could be used. This would still allow for the no-tool geometric freedom AM methods promote and take advantage of the stability and high char of thermoset precursors.

This study did evaluate mass loss with respect to temperature, and shrinkage after pyrolysis, but there is a gap in the relationship of the two. Future work should employ a dilatometer to measure shrinkage in X, Y, and Z orientations to get precise measure of shrinkage rates to combine with TGA mass loss rates, each at discrete temperatures. This would form a more cohesive understanding of the dimensional and mass changes through pyrolysis.

The preforms here demonstrated a predictable shrinkage of about 1% along the fibers and around 20% normal to the fibers, with intra-bead voids carrying over from the PMC state. Some issues with inconsistent pyrolysis, particularly in layers close to the build plate, were noted. Perhaps the most interesting finding is that bulk density of the parts changed less than 1% after pyrolysis. Each of these elements provides insights to guide design for a future designer when selecting a particular density and post-processing procedure for a given application.

Optimization of feedstock and printing parameters is also an important area of further work. Namely the high closed void content of the feedstock is an issue since it creates inaccessible voids that limit ultimate density and strength of CMCs. Feedstock

improvement, print parameter adjustment, and post-processing could all contribute to this. It is also hypothesized that print defects might be a major contributor to partial failure. Determining the print defects which lead to such failure initiation will be a key factor in maturing this technology.

Overall, FFF of discontinuous fiber, thermoplastic matrix precursor ceramic matrix composite preforms has been shown to be viable through the use of an oxygen-dependent, thermo-oxidative stabilization process. Further refinement might one day allow for expansive use of CMCs in high-speed systems and enable the ever increasing demands on such vehicles.

Bibliography

[1] 3DXTech, "Technical data sheet: Carbonx 20viii, 21, 22

[2] E. Fitzer and L. M. Manocha, *Carbon Reinforcements and Carbon/Carbon Composites*. Springer, 1998. ix, 7, 8, 10, 11, 46

[3] L. Yang, Y. Ohki, N. Hirai, and S. Hanada, "Aging of poly(ether ether ketone) by heat and gamma rays — its degradation mechanism and effects on mechanical, dielectric and thermal properties," *Polymer Degradation and Stability*, vol. 142, pp. 117–128, 8 2017. ix, 13, 14, 15, 35

[4] A. Pascual, M. Toma, P. Tsotra, and M. C. Grob, "On the stability of peek for short processing cycles at high temperatures and oxygen-containing atmosphere," *Polymer Degradation and Stability*, vol. 165, pp. 161–169, 7 2019. ix, 13, 14, 15, 31, 32, 35, 48

[5] J. D. Anderson, *Aircraft performance and design*. WCB/McGraw-Hill, 1999. 1

[6] R. P. Hallion, "The history of hypersonics: Or, "back to the future - again and again"," *43rd AIAA Aerospace Sciences Meeting and Exhibit - Meeting Papers*, pp. 12197–12236, 2005. 1

[7] D. M. V. Wie, D. G. Drewry, D. E. King, and C. M. Hudson, "Ultra-high temperature ceramics the hypersonic environment: Required operating conditions and design challenges," *Journal of materials science*, 2004. 2

[8] G. Savage, *Carbon-Carbon Composites*. Springer Netherlands, 1993. 2, 7, 10, 11, 12, 46

[9] D. E. Glass, "Ceramic matrix composite (cmc) thermal protection systems (tps) and hot structures for hypersonic vehicles," 2008. 2

[10] F. Reichert, N. Langhof, and W. Krenkel, "The evaluation of thermoplastic precursors for c/c-sic manufactured by liquid silicon infiltration (lsi)," *Materials Science Forum*, vol. 825-826, pp. 232–239, 2015. 3, 12

[11] L. dos Santos Conejo, H. R. de Meneses Neto, J. B. de Oliveira, L. F. de Paula Santos, R. Z. Nakazato, L. R. de Oliveira Hein, W. Kok, and E. C. Botelho, "Production and characterization of carbon/carbon composites from thermoplastic matrices," *Journal of Polymer Research*, vol. 28, 4 2021. 3, 12

[12] L. M. Manocha, A. Warrier, S. Manocha, D. Sathiyamoorthy, and S. Banerjee, "Thermophysical properties of densified pitch based carbon/carbon materials-ii. bidirectional composites," *Carbon*, vol. 44, pp. 488–495, 3 2006. 3

[13] E. S. Romero, E. Barocio, and R. W. Trice, "Evaluating extrusion deposited additively manufactured fiber-reinforced thermoplastic polymers as carbon/carbon preforms," *Applied Composite Materials*, 11 2023. 3, 12, 17, 19, 35, 37, 40

[14] D. Jiang and D. E. Smith, "Anisotropic mechanical properties of oriented carbon fiber filled polymer composites produced with fused filament fabrication," *Additive Manufacturing*, vol. 18, pp. 84–94, 12 2017. 3

[15] J. N. Francis, I. Banerjee, A. Chugh, and J. Singh, "Additive manufacturing of polyetheretherketone and its composites: A review," 9 2022. 3, 12

[16] A. Das, C. A. Chatham, J. J. Fallon, C. E. Zawaski, E. L. Gilmer, C. B. Williams, and M. J. Bortner, "Current understanding and challenges in high temperature additive manufacturing of engineering thermoplastic polymers," 8 2020. 3

[17] R. Ogle, "Optimized 3d-printing of carbon fiber-reinforced polyether-ether-ketone (cfr-peek) for use in overmolded lattice composite," 2022. 3

[18] J. Sun, D. Ye, J. Zou, X. Chen, Y. Wang, J. Yuan, H. Liang, H. Qu, J. Binner, and J. Bai, "A review on additive manufacturing of ceramic matrix composites," *Journal of Materials Science and Technology*, vol. 138, pp. 1–16, 3 2023. 3, 16, 40

[19] W. Freudenberg, F. Wich, N. Langhof, and S. Schafföner, "Additive manufacturing of carbon fiber reinforced ceramic matrix composites based on fused filament fabrication," *Journal of the European Ceramic Society*, vol. 42, pp. 1822–1828, 4 2022. 3, 11, 12, 17, 18, 19, 21, 24, 40

[20] K. K. Chawla, *Composite materials: Science and engineering, third edition*. Springer New York, 1 2012. 4, 10, 11, 46

[21] J. Cleland and F. Lannetti, "Thermal protection system. of the space shuttle," 1989. 5

[22] H. Aglan, Z. Qian, and D. Mitra-Majumdar, "The effect of temperature on the critical failure properties of advanced polymer composites," 1992. 5

[23] R. Hsissou, R. Seghiri, Z. Benzekri, M. Hilali, M. Rafik, and A. Elharfi, "Polymer composite materials: A comprehensive review," 4 2021. 5

[24] C. G. Papakonstantinou, P. Balaguru, and R. E. Lyon, "Comparative study of high temperature composites," 2001. 5

[25] S. Schmidt, S. Beyer, H. Knabe, H. Immich, R. Meistring, and A. Gessler, "Advanced ceramic matrix composite materials for current and future propulsion technology applications," 8 2004. 5

[26] S. Dhanasekar, A. T. Ganesan, T. L. Rani, V. K. Vinjamuri, M. N. Rao, E. Shankar, Dharamvir, P. S. Kumar, and W. M. Golie, "A comprehensive study

of ceramic matrix composites for space applications," *Advances in Materials Science and Engineering*, vol. 2022, 2022. 6

[27] B. Heidenreich, "C/sic and c/c-sic composites," 2015. 6

[28] F. Christin, "Design, fabrication, and application of thermostructural composites (tsc) like c/c, c/sic, and sic/sic composites," 12 2002. 6

[29] L. C. Pardini and M. L. Gregori, "Modeling elastic and thermal properties of 2.5d carbon fiber and carbon/sic hybrid matrix composites by homogenization method," *Journal of Aerospace Technology and Management*, vol. 2, pp. 183–194, 2010. 7

[30] T. Windhorst and G. Blount, "Carbon-carbon composites: a summary of recent developments and applications," 1997. 7, 10

[31] U. Santhosh, J. Ahmad, T. Easler, and Y. Gowayed, "A polymer infiltration and pyrolysis (pip) process model for ceramic matrix composites (cmcs)," *Journal of the American Ceramic Society*, vol. 104, pp. 6108–6130, 12 2021. 10

[32] X. Wu, N. Langhof, W. Krenkel, R. Habath, and F. Lenz, "Effect of pyrolysis temperature on the microstructure and capillary infiltration behavior of carbon/carbon composites," *Ceramics International*, vol. 44, pp. 16325–16332, 10 2018. 10

[33] F. Kessel, L. Klopsch, V. Jehle, N. J. Biller, M. Frieß, Y. Shi, D. Cepli, M. Keck, and R. Jemmali, "Wet-laid nonwoven based ceramic matrix composites: An innovative and highly adaptable short fiber reinforcement for ceramic hybrid and gradient materials," *Journal of the European Ceramic Society*, vol. 41, pp. 4048–4057, 7 2021. 11

[34] C. L. Cramer, B. Yoon, M. J. Lance, E. Cakmak, Q. A. Campbell, and D. J. Mitchell, "Additive manufacturing of c/c-sic ceramic matrix composites by

automated fiber placement of continuous fiber tow in polymer with pyrolysis and reactive silicon melt infiltration," *Journal of Composites Science*, vol. 6, 12 2022. 11, 17, 18

[35] L. Jin and H. Ishida, "New thermo-oxidative protective coating for carbon/carbon composites in mid-temperature range using a combination of nano-filler and macro-filler with polybenzoxazine as a carbon-forming matrix," *Polymer Composites*, vol. 32, pp. 1164–1173, 8 2011. 11

[36] J. L. White, L. J. Ca, and P. U. S. A. M. Sheaffer, "Pitch-based processing of carbon-carbon composites," 1989. 12

[37] C. A. Love-Baker, T. M. Harrell, A. Scherschel, Z. Gao, N. Song, K. R. Brown, F. Vautard, I. Ivanov, J. Klett, and X. Li, "Unveiling the microstructural evolution of carbon fibers derived from polyamide-6," *Journal of Polymer Research*, vol. 30, 2 2023. 12

[38] F. Reichert, A. M. Pérez-Mas, D. Barreda, C. Blanco, R. Santamaria, C. Kuttner, A. Fery, N. Langhof, and W. Krenkel, "Influence of the carbonization temperature on the mechanical properties of thermoplastic polymer derived c/c-sic composites," *Journal of the European Ceramic Society*, vol. 37, pp. 523–529, 2 2017. 12

[39] F. Reichert, N. Langhof, and W. Krenkel, "Influence of thermal fiber pretreatment on microstructure and mechanical properties of c/c-sic with thermoplastic polymer-derived matrices," *Advanced Engineering Materials*, vol. 17, pp. 1119–1126, 8 2015. 12

[40] T. Liensdorf, N. Langhof, and W. Krenkel, "Mechanical properties of peek-derived c/sic composites with different fiber lengths," *Advanced Engineering Materials*, vol. 21, 5 2019. 12

[41] G. Bianchi, S. Vitullo, A. Vodermayer, and A. Ortona, "Influence of pyrolysis and silicon infiltration on the properties of cmc parts shaped by composite flow molding," *International Journal of Applied Ceramic Technology*, vol. 19, pp. 45–53, 1 2022. 12

[42] M. Pelanconi, P. Colombo, and A. Ortona, "Additive manufacturing of silicon carbide by selective laser sintering of pa12 powders and polymer infiltration and pyrolysis," *Journal of the European Ceramic Society*, vol. 41, pp. 5056–5065, 8 2021. 12

[43] P. Patel, T. R. Hull, R. W. McCabe, D. Flath, J. Grasmeder, and M. Percy, "Mechanism of thermal decomposition of poly(ether ether ketone) (peek) from a review of decomposition studies," 5 2010. 12

[44] A. Ramgobin, G. Fontaine, and S. Bourbigot, "A case study of polyether ether ketone (i): Investigating the thermal and fire behavior of a high-performance material," *Polymers*, vol. 12, 8 2020. 12

[45] A. Ramgobin, G. Fontaine, and S. Bourbigot, "A case study of polyetherether-ketone (ii): Playing with oxygen concentration and modeling thermal decomposition of a high-performance material," *Polymers*, vol. 12, 7 2020. 12

[46] A. R. Zanjanijam, I. Major, J. G. Lyons, U. Lafont, and D. M. Devine, "Fused filament fabrication of peek: A review of process-structure-property relationships," 8 2020. 12, 46

[47] I. V. Panayotov, V. Orti, F. Cuisinier, and J. Yachouh, "Polyetheretherketone (peek) for medical applications," 7 2016. 12

[48] K. C. Cole and L. G. Casella, "Fourier transform infrared spectroscopic study of thermal degradation in films of poly(etheretherketone)," 1992. 13, 15, 35

[49] E. Courvoisier, Y. Bicaba, and X. Colin, "Multi-scale and multi-technique analysis of the thermal degradation of poly(ether ether ketone)," *Polymer Degradation and Stability*, vol. 151, pp. 65–79, 5 2018. 13, 15, 31, 35

[50] D. Gaitanelis, C. Worrall, and M. Kazilas, "Detecting, characterising and assessing peek's and cf-peek's thermal degradation in rapid high-temperature processing," *Polymer Degradation and Stability*, vol. 204, 10 2022. 13

[51] S. Giancaterina, A. Rossi, A. Rivaton, and J. L. Gardette, "Photochemical evolution of poly(ether ether ketone)," 2000. 13

[52] M. Day, J. D. Cooney, and D. M. Wiles, "The kinetics of the oxidative degradation of poly(ar e r-err-stop) (peek) *," 1989. 13

[53] X. Lv, F. Ye, L. Cheng, S. Fan, and Y. Liu, "Binder jetting of ceramics: Powders, binders, printing parameters, equipment, and post-treatment," 7 2019. 16, 17

[54] S. Zakeri, M. Vippola, and E. Levänen, "A comprehensive review of the photopolymerization of ceramic resins used in stereolithography," 10 2020. 16

[55] E. Peng, D. Zhang, and J. Ding, "Ceramic robocasting: Recent achievements, potential, and future developments," 11 2018. 16

[56] J. Best, W. Freudenberg, N. Langhof, and S. Schafföner, "Processing-microstructure correlations in material extrusion additive manufacturing of carbon fiber reinforced ceramic matrix composites," *Additive Manufacturing*, vol. 79, 1 2024. 17, 18, 19, 40

[57] M. R. O'Masta, E. Stonkevitch, K. A. Porter, P. P. Bui, Z. C. Eckel, and T. A. Schaedler, "Additive manufacturing of polymer-derived ceramic matrix composites," *Journal of the American Ceramic Society*, vol. 103, pp. 6712–6723, 12 2020. 19

[58] S. Sommacal, A. Matschinski, K. Drechsler, and P. Compston, "Characterisation of void and fiber distribution in 3d printed carbon-fiber/peek using x-ray computed tomography," *Composites Part A: Applied Science and Manufacturing*, vol. 149, 10 2021. 42, 46

[59] F. Muhammed, T. Lavaggi, S. Advani, M. Mirotznik, and J. W. Gillespie, "Influence of material and process parameters on microstructure evolution during the fabrication of carbon–carbon composites: a review," 11 2021. 45, 46

[60] C. Yang, X. Tian, D. Li, Y. Cao, F. Zhao, and C. Shi, "Influence of thermal processing conditions in 3d printing on the crystallinity and mechanical properties of peek material," *Journal of Materials Processing Technology*, vol. 248, pp. 1–7, 10 2017. 45

[61] P. WANG, B. ZOU, S. DING, L. LI, and C. HUANG, "Effects of fdm-3d printing parameters on mechanical properties and microstructure of cf/peek and gf/peek," *Chinese Journal of Aeronautics*, vol. 34, pp. 236–246, 9 2021. 46

[62] N. van de Werken, P. Koirala, J. Ghorbani, D. Doyle, and M. Tehrani, "Investigating the hot isostatic pressing of an additively manufactured continuous carbon fiber reinforced peek composite," *Additive Manufacturing*, vol. 37, 1 2021. 46

[63] B. J. Johnson, S. M. Pedrotty, S. A. Bouslog, R. A. Hagen, W. J. O, S. N. D, G. S. Larsen, C. L. Cramer, D. E. Morr, S. R. Steffes, M. P. Fritz, P. A. DeTrempe, D. Rocca-Bejar, and D. A. Hoffman, "Steps towards a hypersonic entry test platform," 2024. 48

[64] Y. Wang and Y. F. Zhao, "Investigation of sintering shrinkage in binder jetting additive manufacturing process," 2017. 50

Appendix A

TGA Results

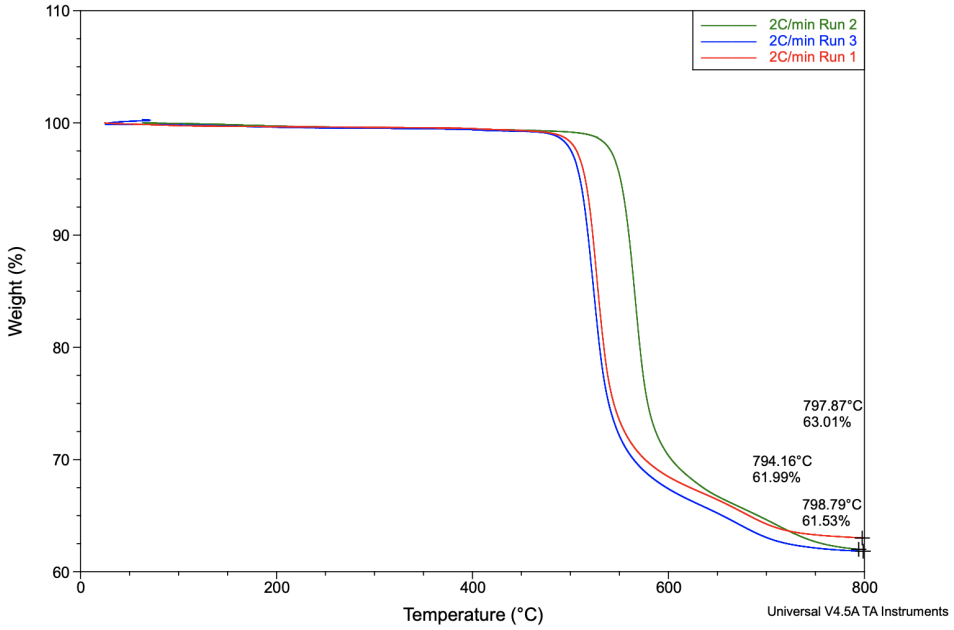

Figure A.1: TGA runs 1, 2, and 3 for feedstock samples run from 400°C to 800°C at 2°C/min.

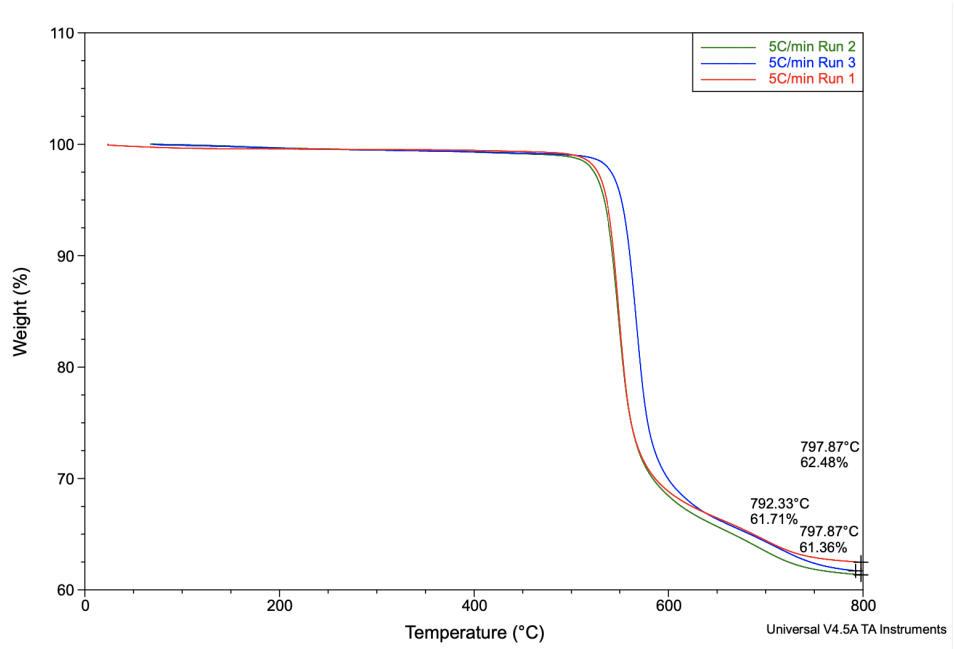

Figure A.2: TGA runs 1, 2, and 3 for feedstock samples run from 400°C to 800°C at 5°C/min.

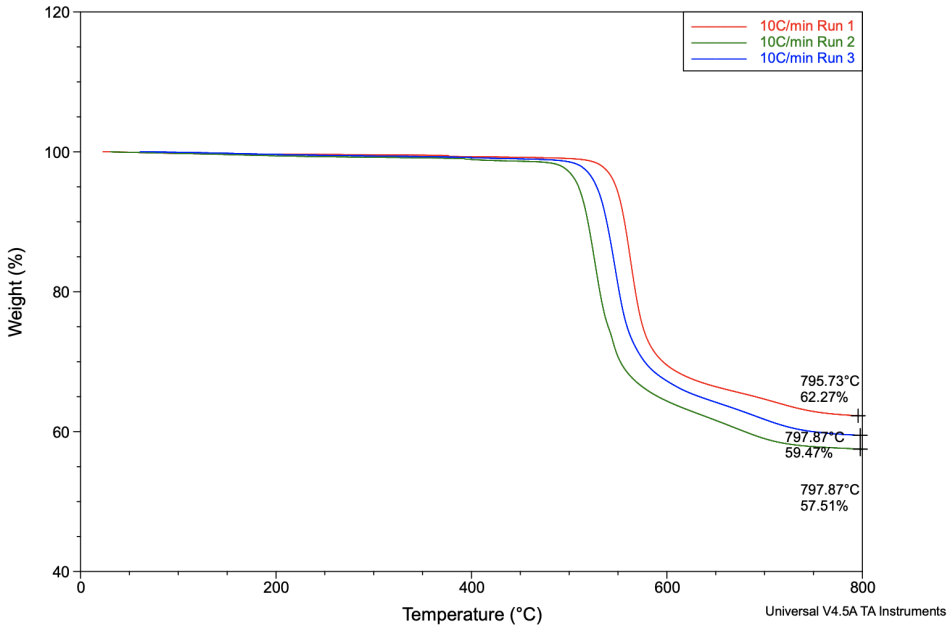

Figure A.3: TGA runs 1, 2, and 3 for feedstock samples run from 400°C to 800°C at 10°C/min.

Appendix B

DSC Results

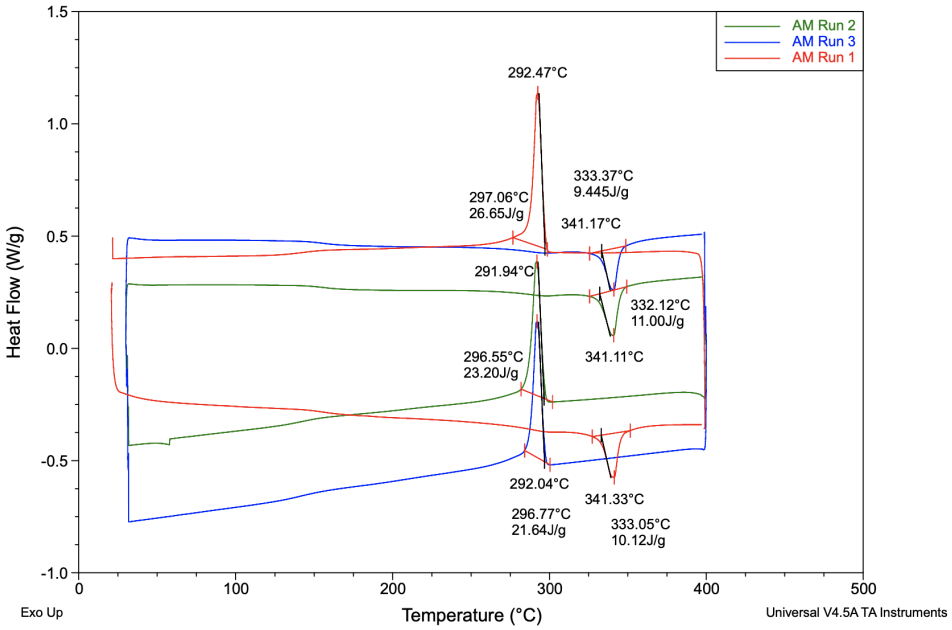

Figure B.1: DSC runs 1, 2, and 3 for individual samples from as-printed cubes to measure melt temperature, melt energy, crystallization temperature, and crystallization energy.

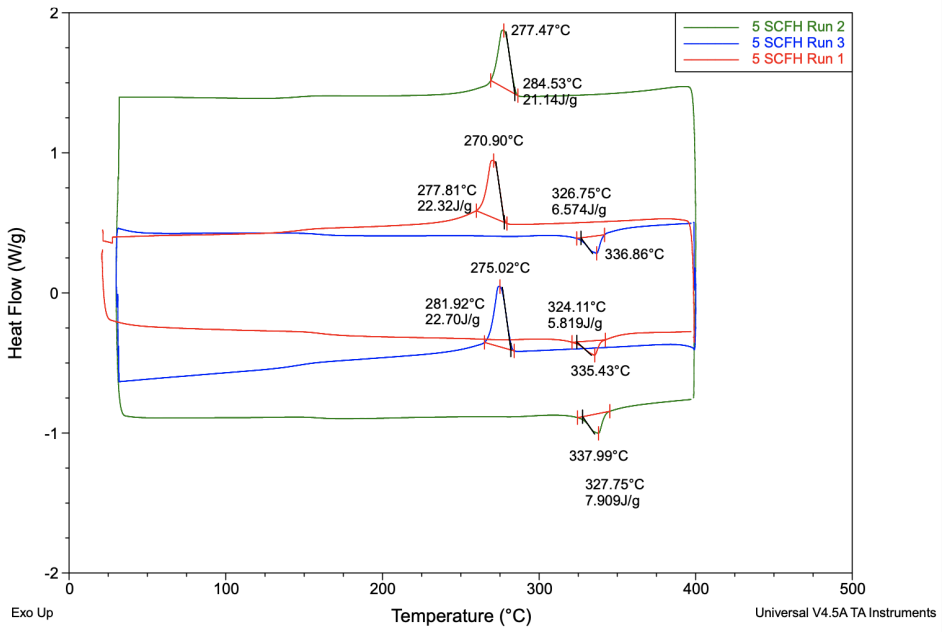

Figure B.2: DSC Runs 1, 2, and 3 for individual samples from 5 SCFH treated cubes to measure melt temperature, melt energy, crystallization temperature, and crystallization energy.

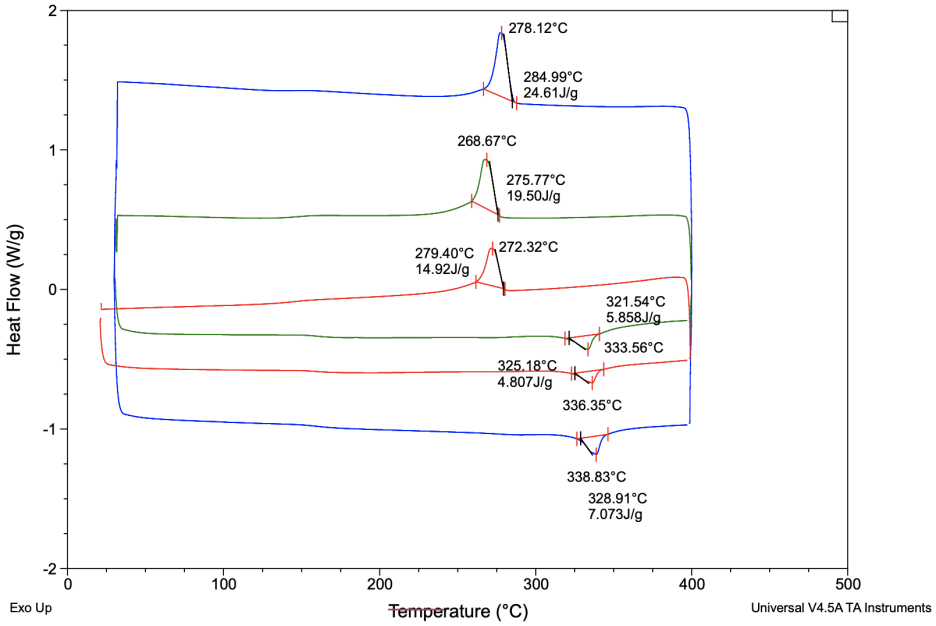

Figure B.3: DSC runs 1, 2, and 3 for individual samples from 10 SCFH treated cubes to measure melt temperature, melt energy, crystallization temperature, and crystallization energy.

Appendix C

DMA Results

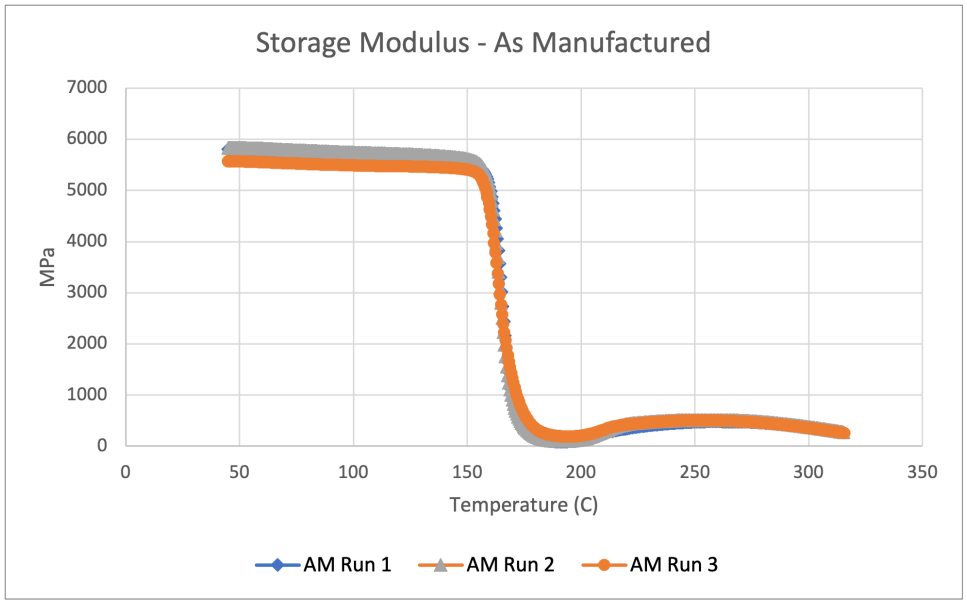

Figure C.1: DMA runs 1, 2, and 3 for as-manufactured samples.

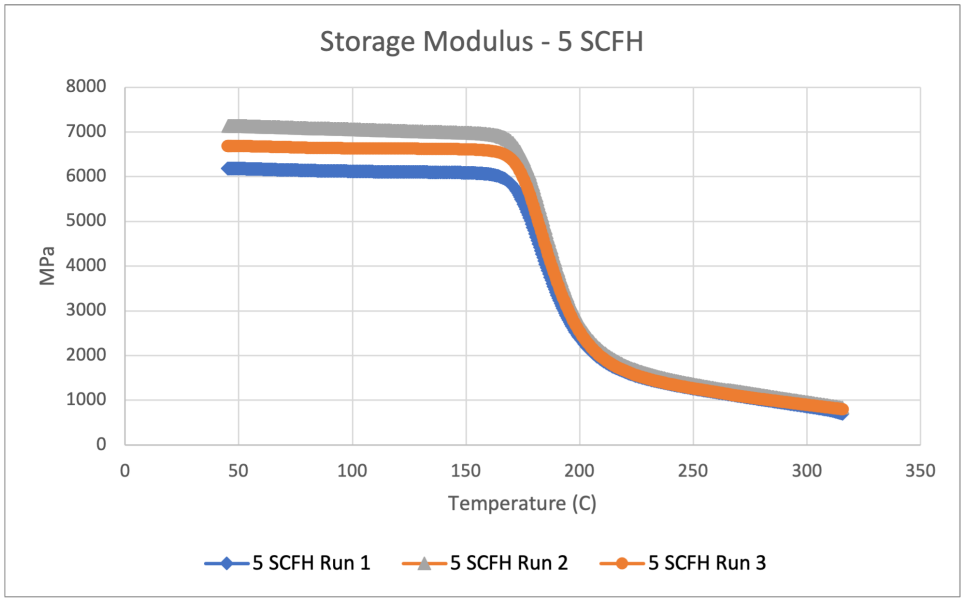

Figure C.2: DMA runs 1, 2, and 3 for 5 SCFH treated samples.

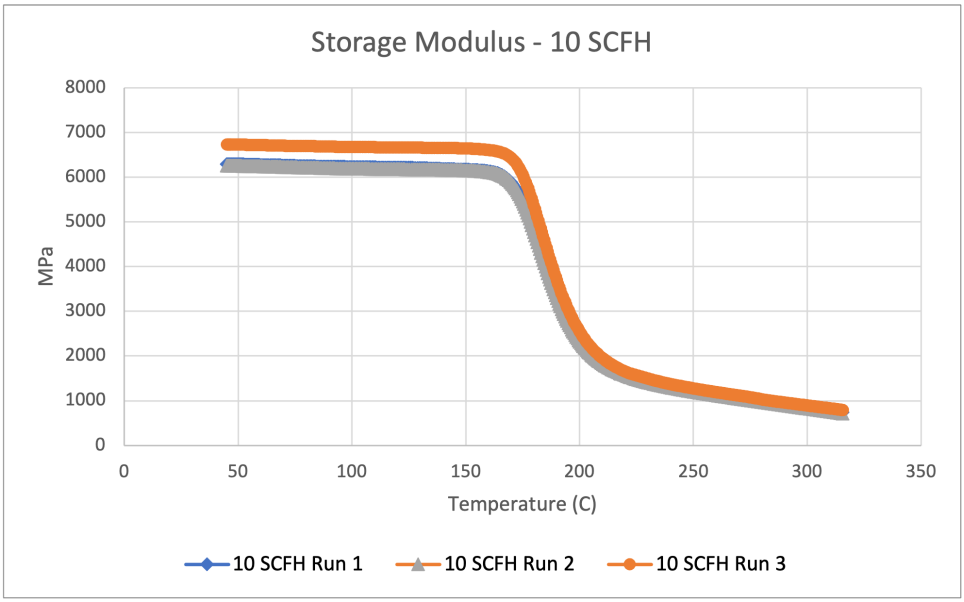

Figure C.3: DMA runs 1, 2, and 3 for 10 SCFH treated samples.

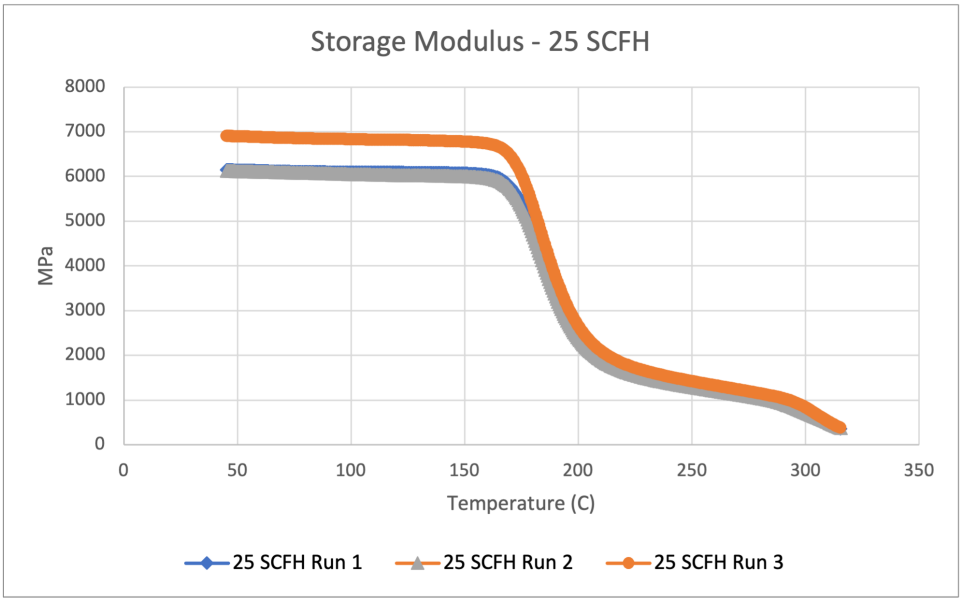

Figure C.4: DMA runs 1, 2, and 3 for 25 SCFH treated samples.

Vita

Samuel Ray Pankratz was born on May 11, 2000 in Knoxville, TN. He was raised in Maryville, TN and took an early interest both in aircraft and building things, leading to the pursuit of a Bachelor of Science degree in Aerospace Engineering at the University of Tennessee, Knoxville. He received his bachelors degree in May 2022, earning departmental awards as an outstanding junior in 2020 and outstanding senior in 2022 along the way. Samuel also represented the college as a Tickle College of Engineering Student Ambassador and was inducted into the Tau Beta Pi engineering honor society during these years. In August 2022, he began his Master of Science work in Mechanical Engineering at the University of Tennessee, Knoxville under the guidance of Dr. Uday Vaidya. During these studies, Samuel collaborated with Oak Ridge National Laboratory and will transition to work in the commercial aerospace manufacturing industry after graduation. He is eternally grateful for the endless support of family and friends through these years of study and transition to his career.